JOURNAL OF MATERIALS SCIENCE 32 (1997) 327–347

Thermal stability of a PCS-derived SiC fibre with a low oxygen content (Hi-Nicalon)

G. CHOLLON, R. PAILLER, R. NASLAIN
Laboratoire des composites Thermostructuraux, 3, allée de La Boétie, 33600 Pessac, France

F. LAANANI, M. MONTHIOUX
Laboratoire Marcel Mathieu, Centre Hélioparc, 2, avenue du Pdt Pierre Angot, 64000 Pau, France

P. OLRY
Société Européenne de Propulsion, 33165 Saint Médard enJalles, France

The oxygen free Si–C fibre (Hi-Nicalon) consists of β-SiC nanocrystals (≈5 nm) and stacked carbon layers of 2–3 nm in extension, in the form of carbon network along the fibre. This microstructure gives rise to a high density, tensile strength, stiffness and electrical conductivity. With respect to a Si–C–O fibre (Nicalon NL202), the Si–C fibres have a much greater thermal stability owing to the absence of the unstable SiO_xC_y phase. Despite its high chemical stability, it is nevertheless subject to a slight structural evolution at high temperatures of both SiC and free carbon phases, beginning at pyrolysis temperatures in the range 1200–1400 °C and improving with increasing pyrolysis temperature and annealing time. A moderate superficial decomposition is also observed beyond 1400 °C, in the form of a carbon enriched layer whose thickness increases as the pyrolysis temperature and annealing time are raised. The strength reduction at ambient for pyrolysis temperatures below 1600 °C could be caused by SiC coarsening or superficial degradation. Si–C fibres have a good oxidation resistance up to 1400 °C, due to the formation of a protective silica layer.

1. Introduction

Silicon carbide fibres are one of the most promising refractory fibres for ceramic matrix composites (CMC's) for high temperature applications in oxidizing atmospheres. In fact, silicon carbide combines (i) excellent mechanical properties up to 1500 °C, such as high strength, stiffness and creep resistance, because of the strength of the Si–C covalent bond and (ii) a rather good oxidation resistance, owing to the formation of a protective silica layer. SiC fibres were first prepared by chemical vapour deposition (CVD). However, these fibres, produced from chemically-deposited SiC on a substrate core, are too large in diameter (100–150 μm) and too stiff to be weavable and their high manufacturing cost precludes volume applications.

In 1975 a breakthrough in SiC fibres production technology was achieved by Yajima *et al.* [1, 2]. Their approach to prepare small diameter continuous fibres involved the spinning of molten polycarbosilane (PCS), the oxygen-curing of the green filaments to make them infusible and their pyrolysis conversion into SiC-based ceramic fibres [1–4]. These fibres are now sold by Nippon Carbon Japan under the tradename Nicalon and they are extensively used for reinforcing polymers, metals, glass and ceramic composites. Nicalon fibres are thermodynamically unstable at high temperatures. This is because the fibre is not composed of pure polycrystalline SiC but instead it consists of small β-SiC crystals (≈2 nm), free carbon and a SiO_xC_y intergranular amorphous material [5–7]. This oxycarbide phase undergoes decomposition above 1100 °C with an evolution of silicon and carbon monoxides which is accompanied by a SiC grain growth [8–16]. This thermal instability results in a degradation of the strength and Young's modulus and limits the maximum temperature of application of the Si–C–O fibres [13–16].

In order to improve the thermal stability of ceramic fibres derived from organosilicon polymers, new routes have been investigated. One approach consists of the introduction of heteroatoms (Ti, N, …) in the ceramic precursor to prevent the SiC crystallization by moving the decomposition temperature towards higher temperatures [17–22]. However, whilst Si–C–N–O and Si–C–Ti–O fibres exhibit a slightly improved thermal stability they are still thermodynamically unstable, since the oxygen curing leads, after pyrolysis, to a silicon oxycarbide (or oxycarbonitride) phase, which undergoes decomposition in the 1200–1400 °C temperature range.

A more promising route is lowering the oxygen content by means of an oxygen-free curing process. The fibres are expected to be much more heat-resistant,

0022–2461

owing to the well-known stability of Si–C (with C: Si(at.) $\geqslant 1$) binary mixtures.

SiC-based fibres (Si–C) with a low oxygen content (< 2 wt %) were prepared by the dry spinning of a high molecular weight PCS solution and subsequent pyrolysis [23]. These fibres displayed a better thermal stability than the Si–C–O Nicalon fibres, i.e., a lower weight loss and a higher residual strength after heat-treatment in argon.

Si–C fibres were also prepared using a chemical vapour curing (CVC) of PCS with unsatured hydrocarbon vapours [24]. These fibres also exhibit a lower weight loss, a better strength retention and a lower grain growth than their oxygen-cured counterparts.

Another original processing route for Si–C fibres has been recently proposed by Lipowitz *et al.* [25–28]. The melt-spun PCS fibres were oxidatively cross-linked with a mixture of NO_2 and BCl_3 and subsequently pyrolysed. Despite some SiC-grain growth and a CO evolution during pyrolysis, dense near-stoichiometric Si–C fibres containing only a few per cent of boron were obtained after firing at temperatures $> 1600\,^{\circ}C$ in argon. This approach can be considered to be similar to conventional sintering (boron being a well known sintering aid for SiC). The fibres have a high strength (σ^R), stiffness (E) and density (close to those of pure SiC) and consist of relatively large β-SiC crystallites, 30–40 nm in size. Limited strength and microstructural change have been observed after a 12 h thermal ageing at $1800\,^{\circ}C$.

Finally PCS-derived fibres have been prepared according to an electron beam irradiation curing process. They have a very low oxygen content (< 0.5 at %) and are reported to retain excellent properties after high temperature heat treatments [29–33]. These fibres are to be commercially available as spools of continuous yarns in the near future.

The aim of this study was to develop a better understanding of the chemical, microstructural and mechanical properties of these fibres as a function of the heat-treatment temperature (HTT).

2. Experimental procedure

2.1. Materials

The Si–C fibres used in these experiments are "Hi-Nicalon" fibres manufactured by Nippon Carbon, Japan. Two batches in the form of tows of approximately 250 filaments were received at different times and finally a spool of continuous fibres coated with polyvinyl acetate (PVA) sizing was provided. Preliminary analysis and characterization tests of the first two batches were performed before a wider study on the third batch was attempted. Chemical analysis by electron probe micro analysis (EPMA) and structural analysis by transmission electron microscopy (TEM) on the fibres showed no significant difference between the three samples. Conversely, the surface analysis of the first two batches revealed a rather thick (50 nm) oxygen and carbon enriched layer and a rough surface, whereas the fibres from the third batch had a smooth surface and a much thinner oxygen-rich layer (≈ 5 nm). No significant differences in the mechanical behaviour (σ^R, E) at ambient temperature was noticed between the fibres. Most of the characterization tests were applied to the third batch.

The PVA sizing of the as-received fibres was removed before analysis. Since classical desizing methods (dissolution by acetone and ethanol mixture or boiling water) were unsuccessful, a short oxidizing treatment in air (3 min at $600\,^{\circ}C$) was performed in order to fully remove the organic coating.

2.1.1. Annealing treatments

Annealing treatments were performed at increasing HTT with a high-temperature pyrolysis apparatus which was composed of a graphite crucible heated with a radio frequency coil. The samples were rapidly heated ($30\,^{\circ}C\,min^{-1}$) and maintained at a given temperature T_p ($1200 < T_p < 2000\,^{\circ}C$) under a static high-purity argon atmosphere (100 kPa) for time periods of t_p ($1h < t_p < 10h$). The Argon used was grade N56 from Alphagaz.

2.2. Characterization techniques

The morphology of the fibres was studied by scanning electron microscopy (SEM) using a Jeol 840S microscope. Elemental analyses were performed on polished cross-sections by electron probe microanalysis (EPMA) using a cameca camebax 75 model in the wave length dispersion mode thallium and phthlate (TAP) crystal for Si K_α and a multilayer pseudo-crystal PCII for (C K_α and O K_α) with standards (SiC and SiO_2) whose compositions were assumed to be stoichiometric. It should be noted that the hydrogen content of the samples cannot be assessed by EPMA. Chemical analysis of the as-received fibres were also investigated using conventional procedures at the service central d'Analyse at CNRS, Vernaison, France.

Auger electron spectroscopy (AES) characterization was performed with a scanning microprobe (Physical Electronics model PHI 5905 AM) equipped with an Ar^+ sputtering gun. The variations of the intensities (peak to peak mode) of the Auger electron peaks (Si-LVV; C-KLL and O-KLL) as a function of the sputtering time were used to draw semiquantitative composition–depth profiles from sample surface (sputtering rate reference: Ta_2O_5).

The hydrogen concentration of the fibres was assessed by elastic recoil detection analysis (ERDA). The samples were irradiated with an incident high energy He^+ beam (2.3 MeV) and the spectrum of the elastic recoil ions was recorded as a function of the depth of the nuclear collisions. From this data it was possible to obtain a quantitative hydrogen concentration–depth profile in the sample.

The structure of the monofilaments was studied at the nanometer scale by high resolution transmission electron microscopy (TEM) using a Philips EM400 microscope. The samples were embedded in an epoxy resin and cut into thin foils with an ultramicrotom. The foils were then set on copper microgrids. The TEM analyses were performed in the bright field (BF),

dark field (DF), lattice fringe (LF) and selected area diffraction (SAD) modes.

The X-ray diffraction (XRD) spectra (Cu-K_α) were recorded using a Siemens D5000 diffractometer for a tow of fibres that had been successively heat-treated at pyrolysis temperatures of 1200, 1400, 1500, 1600 °C for 1 h and 1600 °C for 10 h, and from a second tow heated at 1800 and 2000 °C for 1 h. The axis of the tow was perpendicular to the plane defined by the incident and diffracted X ray beams. The apparent mean grain size (L) of the β-SiC crystalline phase present in the samples was calculated from the width (D) of the (111), (220) and (311) diffraction peaks at midheight, according to the Scherrer equation:

$$L = K\lambda/D\cos\theta \quad (1)$$

where K is a constant (taken as 1), λ the CuK_α wavelength (i.e., $\lambda = 0.154$ nm) and θ the Bragg angle ($\theta = 17.8°$ for β-SiC (111)).

The structural change in the pyrolysed filaments as a function of pyrolysis temperature was also investigated using Raman spectroscopy microanalysis (RSMA) OMARS 89 from Dilor with as a laser source Ar^+, $\lambda = 514.53$ nm, 100 mW, lateral resolution: 1 μm). Analyses were performed either in the middle of the fracture surface or longitudinally, on the fibre surface. Si–C–O (Nicalon) fibres were also analysed as a reference.

Solid state ^{29}Si and ^{13}C nuclear magnetic resonance (NMR) analyses were performed on powder samples for the as-received and heat treated fibres. The spectra were recorded on Brücker ASX100 and ASX500 spectrometers operating at 99.3 MHz for ^{29}Si and at 25.1 MHz for ^{13}C. The samples were spun at 4000–5000 Hz according to the magic angle spinning (MAS) technique.

Electron spin resonance (ESR) experiments were performed with a Varian X-band spectrometer (10^{10} Hz), at room temperature (295 K). The g-value, linewidth, and signal intensity were measured. The number of paramagnetic centres was determined using diphenyl pycryl hydrazil (DPPH) as a standard.

The density of the samples was measured on filament tows using a Accupyc 1330 from Micromeretics.

The thermal stability of the fibres was studied by thermogravimetric analyses (TGA) under inert atmosphere using a TAG24 from Setaram. Experiments were performed on ~100 mg samples, contained in a graphite crucible and progressively heated at a rate of 10 °C per min up to 1800 °C, under flowing high purity argon at a pressure of 100 kPa and a flow rate of 1 l h^{-1}.

The electrical conductivity of the fibres was measured using the four-point method, from room temperature to about −190 °C. A single fibre connected to copper wires with silver paint and glued at the end of a thermocouple, was placed into a glass vessel containing a pure helium atmosphere which was progressively dipped into liquid nitrogen.

The monofilaments were tensile tested at room temperature with an apparatus similar to that described by Villeneuve *et al.* [34]. For each pyrolysis temperature, a batch of about 20 monofilaments was tested using a gauge length of L = 25 mm.

The oxidation kinetics of the Si–C fibres were studied by thermal gravimetric analysis (TGA). The experiments were performed on ~100 mg samples placed in a pure alumina crucible and heated up to a maximum temperature T ranging from 1000–1600 °C (heating rate: 60 °C per min; 10–20 h isothermal plateau at T) under a pure oxygen flow ($P = 100$ kPa; $Q = 1$ l h^{-1}). The silica layer produced in the oxidation was also directly measured on a fracture surface of the filament by means of SEM analysis.

3. Results

3.1. As-received fibres

3.1.1. Chemical analysis

3.1.1.1. Bulk analysis. The average bulk compositions of the as-received fibre measured by conventional and EPMA techniques are shown in Table I. The oxygen content is very low (< 1 at %) with respect to the oxygen-cured fibres Nicalon NL 202 (12–15 O at %). The C:Si ratio (C:Si ≈ 1.41) shows that the Si–C fibre contains free carbon, i.e., 17.5 at % or ≈30 mol %, while in the Si–C–O Nicalon fibre, the amount of free carbon is 14.9 at % or ≈28 mol % [35]. The hydrogen content of the samples was not detected by EPMA. Its weight fraction is assumed to be lower than 0.3 wt % which is the detection limit for elemental analysis (the hydrogen atomic content

TABLE I Composition of as-received Hi-Nicalon, as assessed by (a) conventional chemical analysis and (b) EPMA (that of Nicalon NL202 is also shown for the purpose of comparison)

	Si	C	O	H	C/Si (at)	Free-C (at %)	Free-C (mol %)
Hi-Nicalon (wt %)[(a)]	61.8	37.2	0.6	< 0.3	–	–	–
Hi-Nicalon (at %)[(a)]	41.3/ 39.1	58.0/ 54.9	0.7	0/5.3	1.40	17.1/ 16.2	29.2
Hi-Nicalon (at %)[(b)]	41	58	1	–	1.41	17.5	29.9
Nicalon NL202 (at %)[(b)]	39.5	48.5	12	–	1.23	14.9	27.5

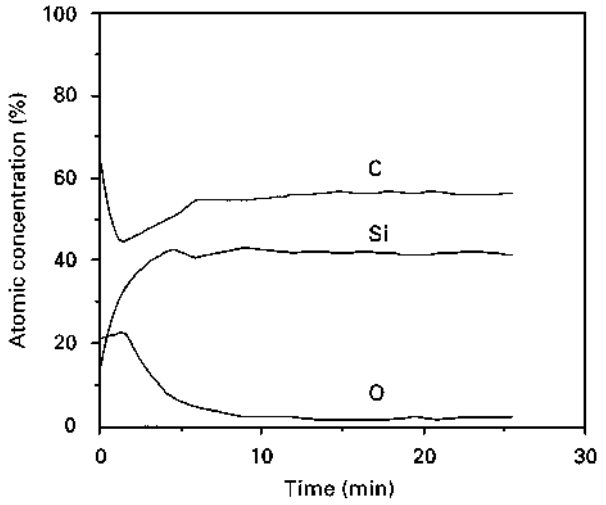

Figure 1 AES semi-quantitative analysis of the surface of the Hi-Nicalon fibre desized 3 min in air at 600 °C. Sputtering rate: 3 nm/min reference Ta_2O_5.

might be thus rather significant, since 0.3 wt % would correspond to 5.3 at %).

As a matter of fact, Gerardin *et al.* have shown by ^{1}H NMR analysis of a PCS pyrolysed at 1200 °C under argon that the residual hydrogen content was 0.27 wt %, which corresponds to 4.9 at % [36]. In our experiments the hydrogen concentration was measured by ERDA. The atomic concentration profile was recorded from the surface to a depth of 400 nm. The hydrogen content is constant between 200–400 nm with an apparent average value of $C_H = 0.062$ at % (standard deviation: 0.014 at %). Considering the very low hydrogen concentration measured by ERDA, (close to the detection limit), one might assume that the actual concentration could be lower or even nil. As a matter of fact (as it will be discussed in Section 3.2), the decrease of the hydrogen content has been shown by ERDA to occur after the heat treatments which corroborates the occurrence of at least some low residual hydrogen concentration in the as-received fibre.

3.1.1.2. Surface analysis. The AES depth profiles of the Si–C fibre (Fig. 1) show a thin oxygen-enriched layer ($\approx$5 nm) near the surface. This layer is thought to be related to the desizing treatment. Its thickness is much lower than that reported by Bodet *et al.* for similar fibres [37].

3.1.2. Morphology

Fracture surfaces of the as-received fibres are shown in Fig. 2 (a and b). Generally speaking, Hi-Nicalon fibres have a smooth surface and exhibit a typical brittle material fracture surface. Internal (Fig. 2a) or external (Fig. 2b) flaws are visible on the micrographs, surrounded by a mirror zone, as it is generally observed for ceramic fibres.

3.1.3. Structural analyses

3.1.3.1. TEM analysis. Fig. 3 (a–d) shows the BF, the SiC_{111} and C_{002} DF images recorded near the fibre

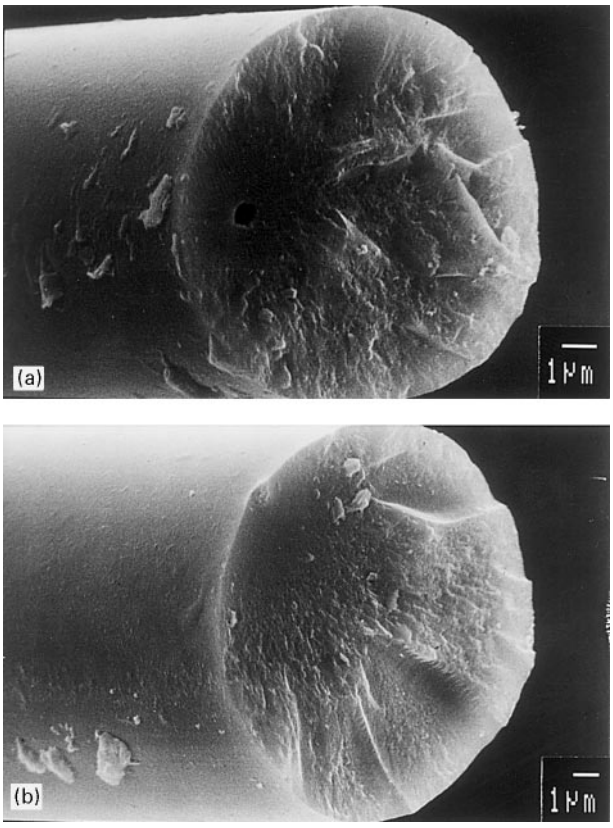

Figure 2 Fracture surfaces of Hi-Nicalon fibres tested at room temperature, showing (a) internal and (b) external flaws. For (a) $\sigma_f = 2160$ MPa and for (b) $\sigma_f = 2360$ MPa.

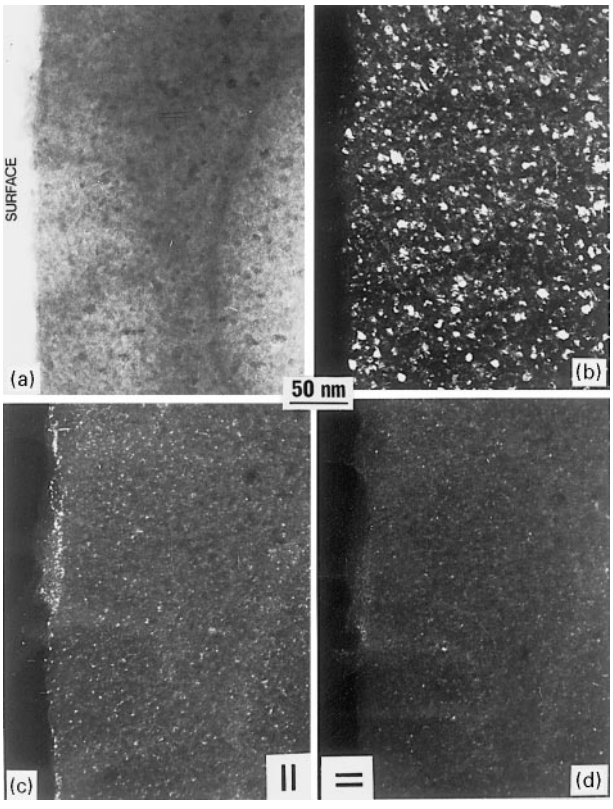

Figure 3 TEM micrographs of the surface of as-received Hi-Nicalon fibre. (a) Bright field, (b) 111-SiC dark field, (c) 002-C dark field and (d) the same, showing aromatic layers orthogonal to those observed in (c).

surface. The SiC grain size is about 2–17 nm (Fig. 3b). The size distribution histogram is yet to be obtained, and will be published later [38] thus the real mean size value is not currently available. However, the model class (i.e., the size class with the highest frequency) can be estimated to be 5 nm for the Si–C Hi-Nicalon fibre versus 1 nm for the Si–C–O Nicalon NL202 fibre ($\approx$1.5–2 nm for the mean size value) [5, 7]. Slight differences in the grain size distribution between inner and outer parts of the fibre are suspected. Indeed a skin/core effect can be evidenced in some SiC_{111} DF images, i.e., larger crystals are less numerous within a 150–200 nm thick surface zone (Fig. 4b).

The C_{002} DF images show a thin polyaromatic carbon layer at the fibre surface (also detected by X-ray photoelectron spectroscopy (XPS) [38]), whose texture is anisotropic, with an orientation parallel to the surface (Fig. 3 (c and d)). Small turbostratic carbon stacks are also visible within the fibre as small nanometric bright dots (Fig. 3 (c and d)). The SAD pattern shows three main rings, corresponding to the 111, 220 and 311 β-SiC Bragg reflections (Fig. 4a). These rings are sharp and even punctuated, which is consistent with the fact that crystals are relatively large. Infrequently, features corresponding to polytypism are observed.

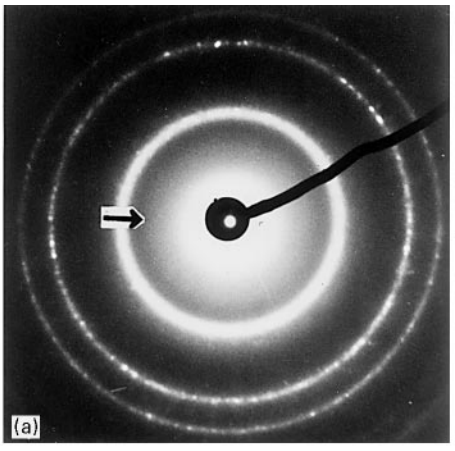

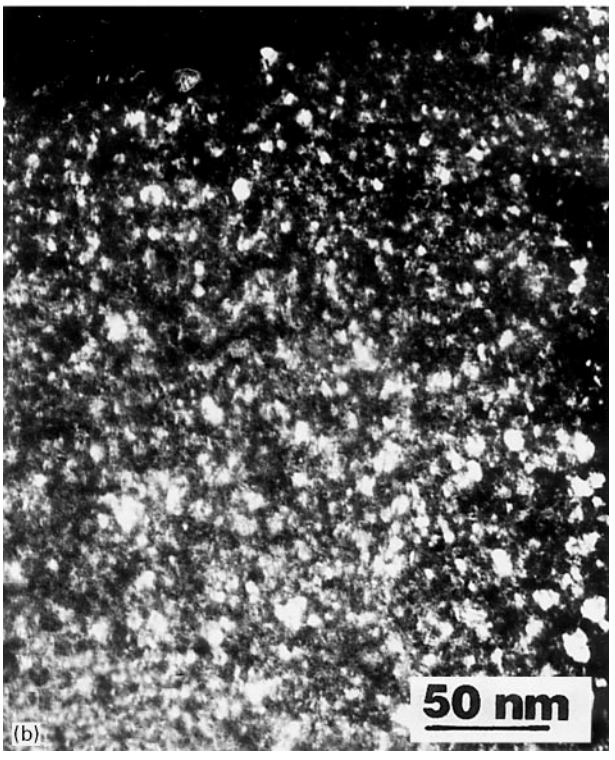

Figure 4 TEM micrographs of as-received Hi-Nicalon fibre. (a) SAD pattern from the bulk, (b) 111-SiC dark field from the surface and the bulk.

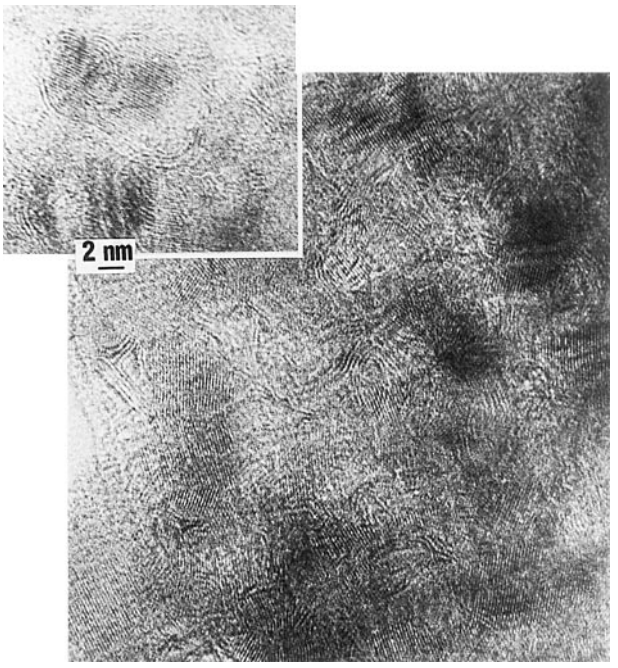

Figure 5 HRTEM micrograph of as-received Hi-Nicalon fibre.

Unlike the Si–C–O fibres, the C_{002} reflection is also easily observed on the SAD pattern (arrow in Fig. 4a), in the form of a weak diffuse ring.

Lattice fringe imaging gives information about the organization of free carbon (Fig. 5). Generally speaking it is better organized than in the Si–C–O (NL202) fibre [7]. Aromatic stacks are about 2–3 nm in extension (versus $\approx$1 nm in the Si–C–O fibre) and the number of stacked layers is close to 5, but 7 to 8 layer stacks could also be observed (versus 2 to 3 in the Si–C–O fibre). As already observed for pyrolysed PCS, the polyaromatic stacks are often associated edge-to-edge between the SiC grains where they form a network of uncompleted cages around SiC crystals.

Lattice fringe imaging also suggest that natural sintering between SiC crystals could exist (circled area in Fig. 5).

3.1.3.2. XRD analysis. The XRD pattern of the as-received Si–C fibre shows three main peaks which were assigned to the (111) ($2\theta = 35.7^\circ$; $d = 0.251$ nm), (220) ($2\theta = 60.0^\circ$; $d = 0.154$ nm) and (311) ($2\theta = 72.0^\circ$; $d = 0.131$ nm) reflections of β-SiC (Fig. 6b) as already observed in the SAD TEM pattern. Two other weak peaks are also observed, which are indexed as the (200) and (222) β-SiC reflections. With respect to the Si–C–O fibres pattern, the narrowness of the peaks suggests a better crystalline state for the β-SiC phase in the Si–C fibre (Fig. 6a). As a matter of fact, the average SiC crystal size determined by the

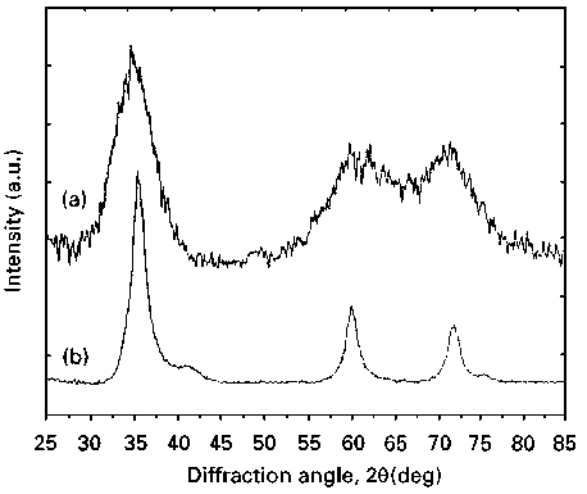

Figure 6 XRD spectra of (a) ceramic-grade Nicalon (Si–C–O) and (b) Hi-Nicalon (Si–C) fibres.

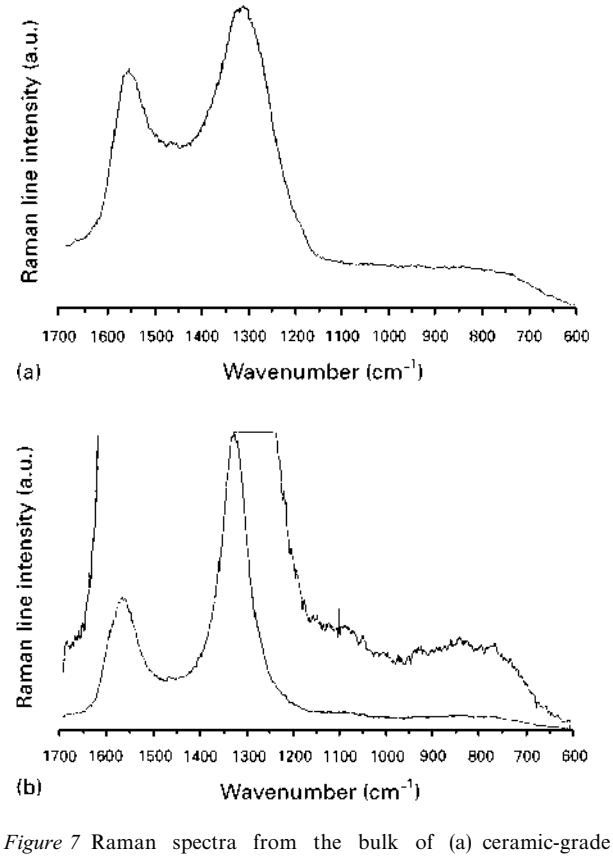

Figure 7 Raman spectra from the bulk of (a) ceramic-grade Nicalon (Si–C–O) and (b) Hi-Nicalon (Si–C) fibres.

Scherrer equation is about 5 nm, in good agreement with the TEM observations. On the other hand, no peak corresponding to turbostratic carbon is observed ($\approx 2\theta = 26.5°$; $d_{C002} = 0.336$ nm).

3.1.3.3. Raman spectroscopy analysis. Raman spectroscopy is a useful technique for the study of structural ordering in materials with a low crystalline state, and especially carbon [39–41] or free-carbon containing materials [42–45]. The Raman spectrum of the as-received fibre shows two peaks at 1350 and 1600 cm^{-1} (Fig. 7b). These bands correspond to the typical vibration frequencies observed in carbon materials. The first (1350 cm^{-1}) is generally assigned to the

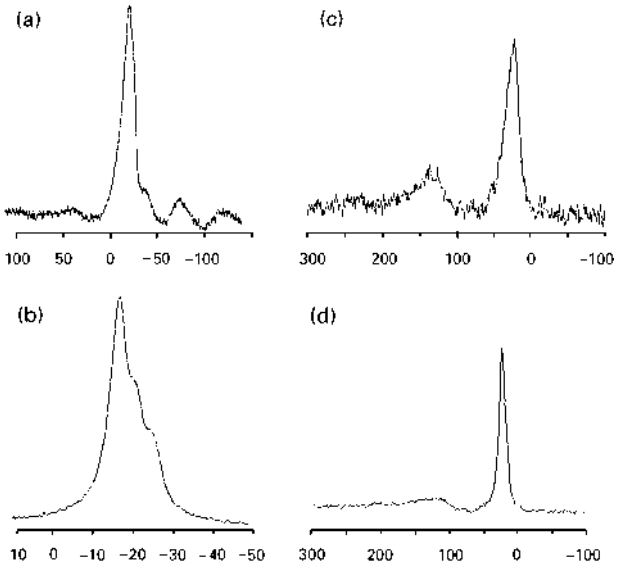

Figure 8 Solid state NMR spectra of (a) ^{29}Si for Si–C–O fibre (Nicalon NL 202), (b) ^{29}Si for Si–C fibre (Hi-Nicalon), (c) ^{13}C for Si–C–O fibre and (d) ^{13}C for Si–C fibre.

"unorganized" carbon, involving lattice defects while the other (1600 cm^{-1}) is due to the E_{2g2} symmetric mode vibration in graphite.

For the Si–C–O fibre (Nicalon NL 202), these two bands are intense and broad, which is similar to the spectra reported by other authors [44, 45] (Fig. 7a). On the other hand, the peaks observed in the Si–C fibre spectrum are narrower and better separated. The peak intensity ratio is also different between the two types of fibres. The I_{1350}/I_{1600} ratio is close to 1.35 for the Si–C–O fibres whilst it is equal to 2 for the Si–C fibre.

A very broad and weak band at about 700–1000 cm^{-1} is apparent in the spectrum which could be assigned to SiC [41–46].

3.1.3.4. Solid state NMR analysis. The ^{29}Si MAS-NMR spectrum of the Si–C–O fibre (Fig. 8a) shows four broad lines centred at −16, −35, −75 and −110 ppm, whilst only one line is observed for the Si–C fibre (Fig. 8b), centred at −16 ppm. The lines can be assigned to five possible tetrahedral structures: SiC_4 (−16 ppm), SiC_3O (≈0 ppm), SiC_2O_2 (−35 ppm), $SiCO_3$ (−75 ppm) and SiO_4 (−110 ppm). In fact, the line centred at −16 ppm can be decomposed into three components, respectively at −16, −19 and −23 ppm (Fig. 8b).

The ^{13}C MAS-NMR spectrum of the Si–C–O fibre shows two broad lines at 20 and 130 ppm (Fig. 8c) which are assigned respectively to the CSi_4 tetrahedral structure and graphite-like polyaromatic structure. These two peaks are also observed for the Si–C fibre but (i) the linewidth of the peak centred at 20 ppm is much lower than that of the Si–C–O fibre and (ii) the second peak is apparently slightly shifted towards lower values (maximum at 120 ppm) (Fig. 8d). Furthermore, one should note that the line at 20 ppm can be decomposed into two components at 16 and 23 ppm.

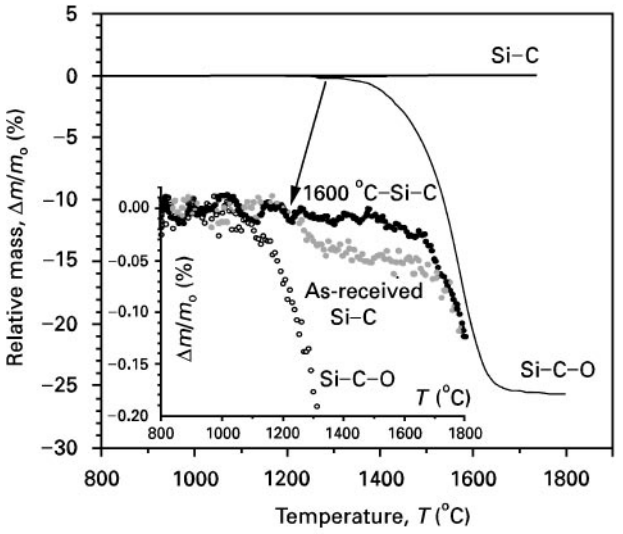

Figure 9 Weight loss curves under argon (100 kPa) for as-received and 1600 °C heat treated Si–C (Hi-Nicalon) fibres and Si–C–O (Nicalon NL202) fibres, as a function of temperature (heating rate: 10 °C per min).

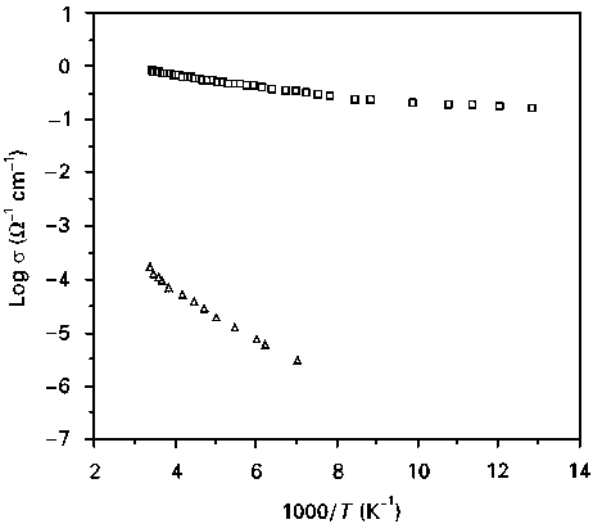

Figure 10 Thermal behaviour of the electrical conductivity of (□) as-recieved Si–C (Hi-Nicalon) and (△) Si–C–O (NL202) fibres.

3.1.4. Density

The density value of the fibre ($d = 2.77\ g\,cm^{-3}$) is slightly higher than that of the Si–C–O fibres ($d_{Si-O-C} = 2.56\ g\,cm^{-3}$) but still far from the pure SiC density ($d_{SiC} = 3.2\ g\,cm^{-3}$).

3.1.5. Thermogravimetric analyses under inert atmosphere

The variations of the relative mass ($\Delta m/m_0$) of the as-received Si–C fibres (Fig. 9) as a function of temperature show only a very slight loss ($\approx 0.12\,\%$) at 1800 °C which demonstrates the improved thermal stability of the oxygen-free fibre with respect to the Si–C–O fibre ($\Delta m/m_0 \approx 25\%$ at 1800 °C).

3.1.6. Electron spin resonance (ESR)

The ESR experimental data are listed in Table II for the as-received and heat-treated fibres (1600 °C/1h/Ar). The g-values are similar to those reported for carbon materials (i.e., almost that for the free electron $g = 0.0023$), and for Si–C–O (Nicalon NL 202) [48, 49] or experimental Si–C–N–O fibres [48]. The paramagnetic susceptibility (χ_p) and the linewidth (S) are also close to those reported by other authors for Si–C–O fibres.

3.1.7. Electrical conductivity

The electrical conductivity (σ) at ambient of the Si–C fibre is four decades higher than that of Si–C–O fibre (Nicalon NL 202) ($\sigma_{Si-C} \approx 0.8\ \Omega^{-1}\,cm^{-1}$ versus $\sigma_{Si-C-O} \approx 10^{-4}\ \Omega^{-1}\,cm^{-1}$). It is observed to increase with temperature over the range −190–25 °C) (Fig. 10) and displays a semi-conducting type behaviour.

3.1.8. Mechanical properties at ambient

The mechanical properties (σ^R and E) have been determined at ambient on as-received fibres, desized in air ($L_0 = 25$ mm, $\Delta l = 0.25\ mm\,min^{-1}$). The tensile strength is high ($\sigma^R = 3060$ MPa) and close to that of the Si–C–O fibre. It is not affected by the desizing

TABLE II ESR data at ambient for as-received and annealed Si–C (Hi-Nicalon) and Si–C–O (Nicalon NL202) fibres

Samples	g	S ($\times 10^{-4}$ T)	χ_p (uem CGS·g^{-1})	N (spin·g^{-1})
Hi-Nicalon (present work)	2.0028	3.8	3.3×10^{-8}	15.5×10^{18}
Hi-Nicalon (1600 °C/1 h/Ar) (present work)	2.0027	2.7	0.65×10^{-8}	3.1×10^{18}
Nicalon NL200 [48]	–	1.5	4.7×10^{-8}	–
Nicalon NL200 [49]	2.0027	2.6	–	–
Nicalon NL200 (1200 °C/N_2) [48]	–	3.35	0.68×10^{-8}	–

treatment. The Young's modulus is much higher than that of the Si–C–O fibres ($E_{Si-C} = 285$ GPa versus $E_{Si-C-O} \approx 200$ GPa).

3.1.9. Oxidation resistance under dry oxygen

3.1.9.1. Oxidation kinetics. A weight increase of the fibres is observed whatever the testing temperature, whose rate increases as the temperature is raised. As already observed for similar materials, the TGA curves are parabolic for $T \leqslant 1400\,^{\circ}C$ (Fig. 11). Assuming that the density and the chemical composition of both fibre core and silica layer remain constant during the test, the thickness of the silica can be inferred from the weight variations.

Under these assumptions the thickness (e) of the oxide can be calculated as a function of time (Fig. 12) from the TGA data according to the following equation (see appendix):

$$e \approx \frac{1}{2} \cdot r_0 \cdot \frac{M_{SiO_2} \cdot C_{Si}}{M_{SiO_2} \cdot C_{Si} - M_{Si}} \cdot \frac{d}{d_{SiO_2}} \cdot \frac{\Delta m}{m_0} \qquad (1)$$

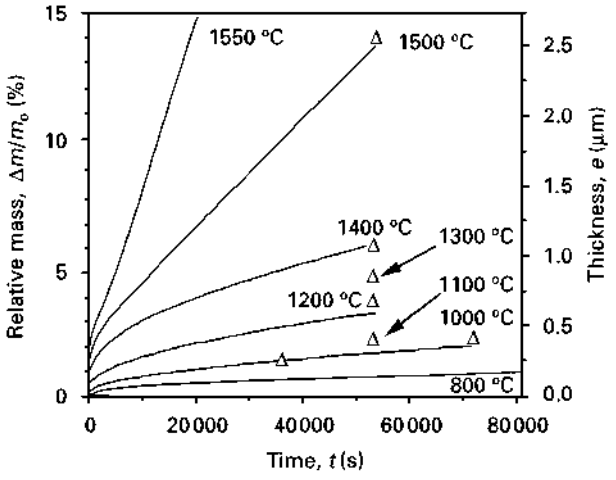

Figure 11 Relative mass and calculated silica thickness variations versus time during oxidation of Hi-Nicalon fibres under flowing dry oxygen between 800 and 1550 °C (P = 100 kPa) ((△) direct SEM measurements).

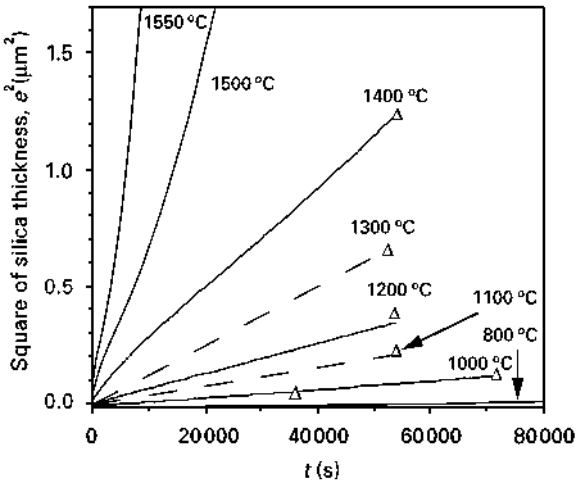

Figure 12 Calculated square of silica thickness variations versus time during oxidation of Hi-Nicalon fibres under flowing dry oxygen between 800 and 1550 °C (P = 100 kPa) ((△) direct SEM measurements).

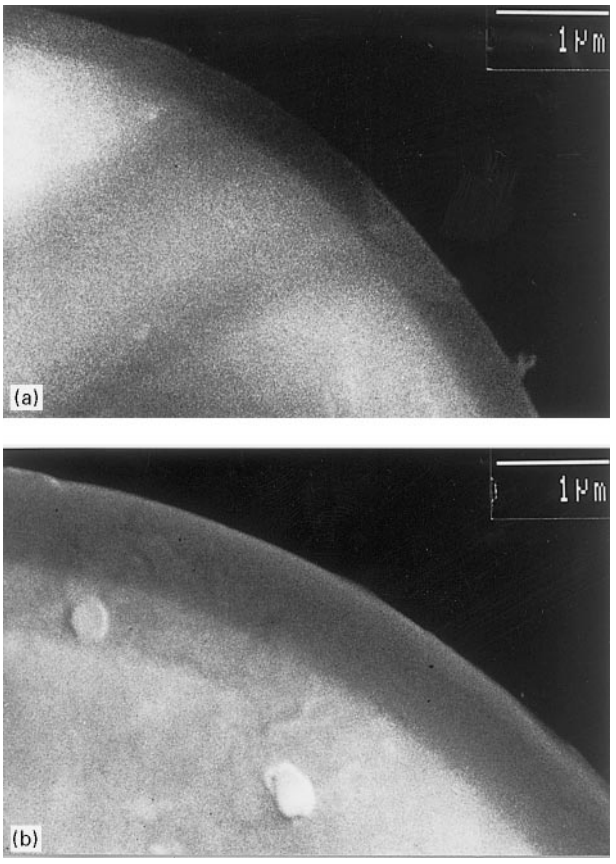

Figure 13 SEM micrographs (backscattered electron mode) of the failure surfaces of oxidized Hi-Nicalon fibres in pure oxygen (100 kPa). (a) $T = 1100\,^{\circ}C$, $t = 15$ h and (b) $T = 1300\,^{\circ}C$; $t = 15$ h.

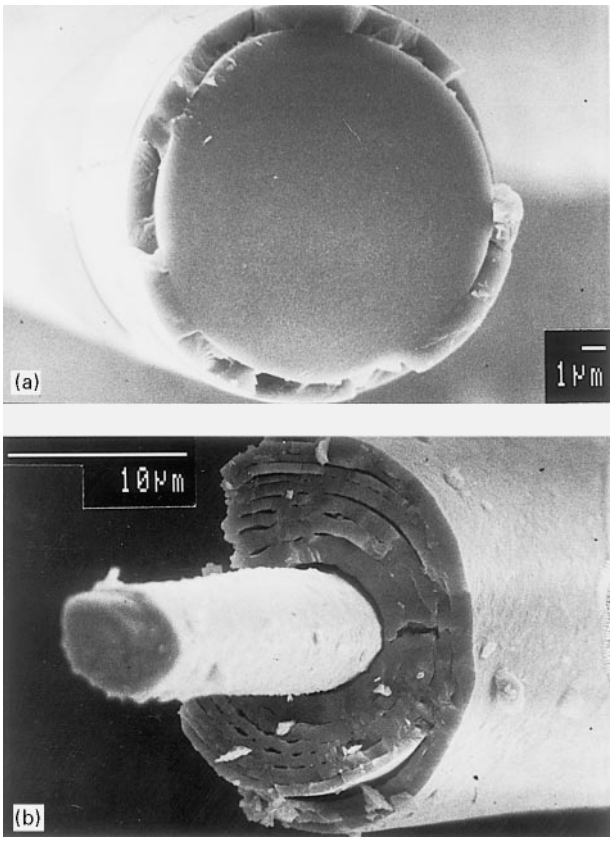

Figure 14 SEM micrographs (secondary electron mode) of the failure surfaces of oxidized Hi-Nicalon fibres in pure oxygen (100 kPa). (a) $T = 1400\,^{\circ}C$, $t = 15$ h and (b) $T = 1550\,^{\circ}C$; $t = 10$ h.

TABLE III Silica thickness data derived from measurements (e_m) or calculated from TGA-curves (e_{cal}), for Hi-Nicalon Si–C fibres

T (°C)	1000	1000	1100	1200	1300	1400	1500
t (h)	10	20	15	15	15	15	15
e_m (μm)	0.25	0.35	0.45	0.65	0.80	1.10	2.6
e_{cal} (μm)	0.24	0.35	–	0.59	–	1.10	2.48

TABLE IV Parabolic law constants e_0 and K_T for the oxidation of Hi-Nicalon Si–C fibres

T (°C)	1000	1200	1400	1500	1550
e_0 (μm)	0.022	0.095	0.176	0.218	0.289
K_T ($\mu m^2 s^{-1}$)	1.8×10^{-6}	6.2×10^{-6}	2.1×10^{-5}	5.7×10^{-5}	8.9×10^{-3}

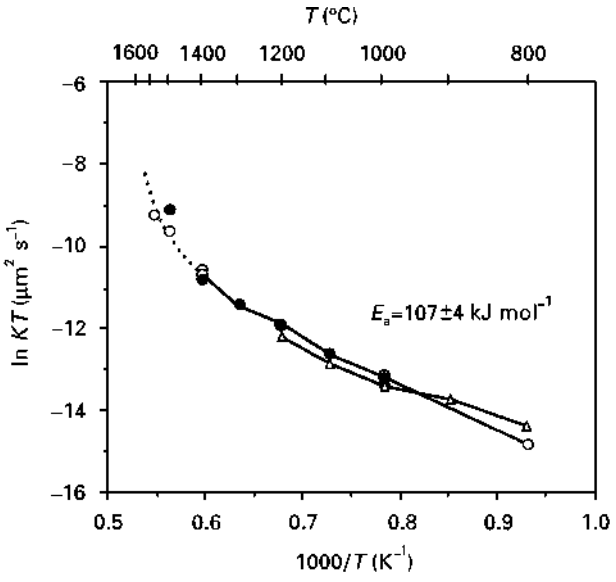

Figure 15 Thermal variations of the oxidation parabolic rate constants for different ex-PCS fibres: (△) Si–C–O fibres (Nicalon NL 202) [68], (●; ○) Si–C fibres (Hi–Nicalon), from SEM measurements and TGA data respectively.

Furthermore the thicknesses of the silica layers were also directly measured by SEM analysis in order to validate Equation 1 (Figs 13 and 14) (Table III).

Similar to $\Delta m/m_0$, the silica thickness obeys a parabolic law for $T \leqslant 1400\,^{\circ}C$ (Fig. 12) which can be written as:

$$e^2(t) - e_0^2 = K_T \cdot t \qquad (2)$$

where K_T is the kinetic constant and e_0 is the silica layer for $t = 0$ (Table IV).

The kinetic constant K_T obeys an Arrhenius equation for $T \leqslant 1400\,^{\circ}C$, as is shown in Fig. 15:

$$\ln K_T = \ln K_\infty - \frac{E_a}{RT} \qquad (3)$$

with $K_\infty = 5\times10^{-2}\ \mu m^2\,s^{-1}$ and $E_a = 107 \pm 4\ kJ\,mol^{-1}$.

For $T > 1400\,^{\circ}C$, the parabolic law is no longer valid except for very short periods of time. A linear variation of the thickness with time is observed for $T = 1500\,^{\circ}C$ beyond $t = 1.5\times10^{-4}\,s$, and a more complex growth behaviour for $T = 1550\,^{\circ}C$.

SEM micrographs of the failure surfaces of oxidized fibres are shown in Figs 13 and 14. For a temperature range of 1000–1400 °C the filaments are coated with a smooth and continuous oxide scale whose thickness

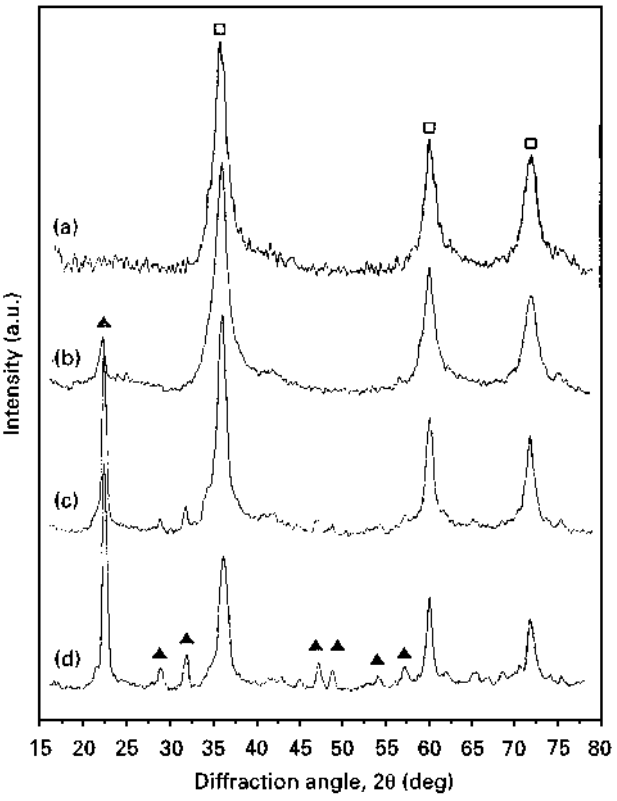

Figure 16 XRD spectra of Hi-Nicalon fibres, as a function of oxidizing temperature (T) and duration (t), in pure oxygen (100 kPa). (a) $T = 1000\,^{\circ}C$, $t = 20$ h; (b) $T = 1200\,^{\circ}C$, $t = 15$ h; (c) $T = 1400\,^{\circ}C$, $t = 15$ h and (d) $T = 1500\,^{\circ}C$, $t = 15$ h. The peaks are assigned to; (□) βSiC or (▲) αSiO_2.

is constant along their whole periphery. For temperatures greater than 1400 °C and long durations, the oxide layers are very thick (several μm) and consist of concentric debonded sheaths (Fig. 14). Cracks are also observed within the oxide scale at these temperatures.

In addition to the β-SiC diffraction peaks, the XRD patterns of oxidized fibres show α-cristobalite peaks that appear at temperatures as low as 1200 °C, and whose intensity increases strongly with the temperature (Fig. 16).

3.2. Properties of the heat-treated fibres at ambient temperature

3.2.1. Chemical analysis

3.2.1.1. Bulk composition. EPMA data show that the composition of the fibre is unchanged for pyrolysis temperatures upto 1800 °C (Table V). At 2000 °C, the oxygen content is significantly reduced to a negligible level and the carbon concentration seems to be slightly increased. These data confirm the very high thermal stability of the fibre under an inert atmosphere. An ERDA analyses performed near the fibre surface (200–400 nm depth zone) showed that the apparent hydrogen amount is progressively reduced with increasing pyrolysis temperature (Table VI).

3.2.1.2. Surface analysis. A slight evolution of the surface of the filament is observed when the annealing temperature is increased. For $T_p = 1200\,^{\circ}C$ and $t_p = 1$ h, the oxygen enriched layer observed for the

TABLE V Elemental composition of Hi-Nicalon fibres treated at increasing temperatures, as assessed by EPMA

T_p (°C)	Si (at %)	C (at %)	O (at %)
As-received	41.2	58.0	0.8
1200 (1 h)	40.7	58.3	1
1400 (1 h)	40.9	58.2	0.9
1600 (1 h)	40.3	58.8	0.9
1600 (10 h)	40.0	58.9	1.1
1800 (1 h)	41.0	58.1	0.9
2000 (1 h)	39.6	60.1	0.3

TABLE VI Hydrogen content of Hi-Nicalon fibres as assessed by ERDA

	as-received	$T_p = 1400$°C	$T_p = 1600$°C
Apparent hydrogen concentration (at %)	0.062	0.051	0.043
Standard deviation (at %)	0.014	0.016	0.014

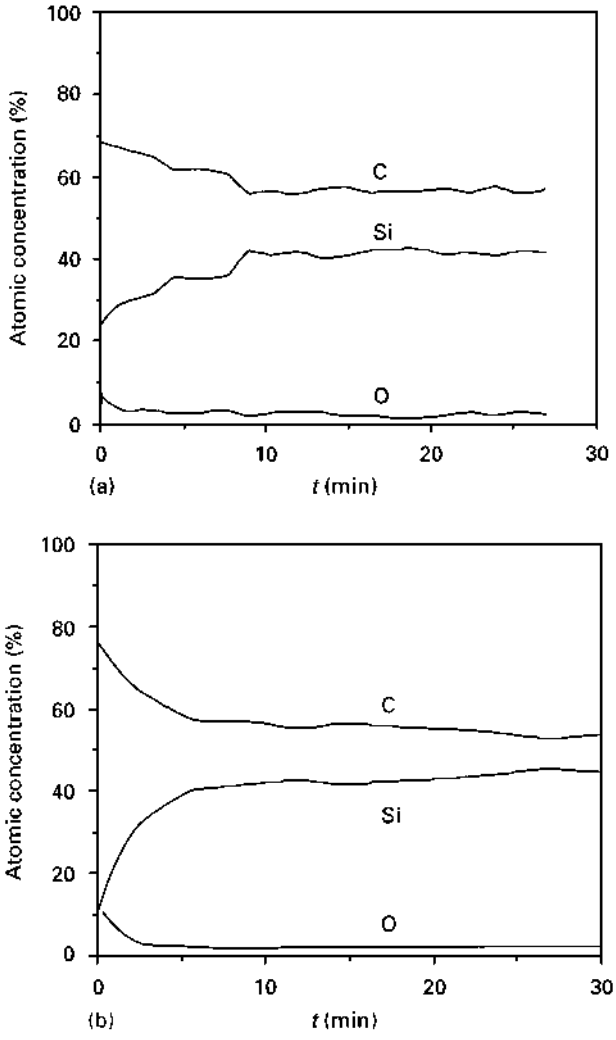

Figure 17 AES semi-quantitative analysis of the surface of Hi-Nicalon fibres heat-treated under pure argon (100 kPa), for increasing duration ($T_p = 1600$ °C) (sputtering rate: 5nm per min. reference Ta_2O_5. (a) $t_p = 1$ h and (b) $t_p = 10$ h.

desized untreated fibres has almost disappeared and the composition of the surface is nearly the same as that of the core. A thin carbon layer appears at 1400 °C (≈ 10 nm) and continuously grows with

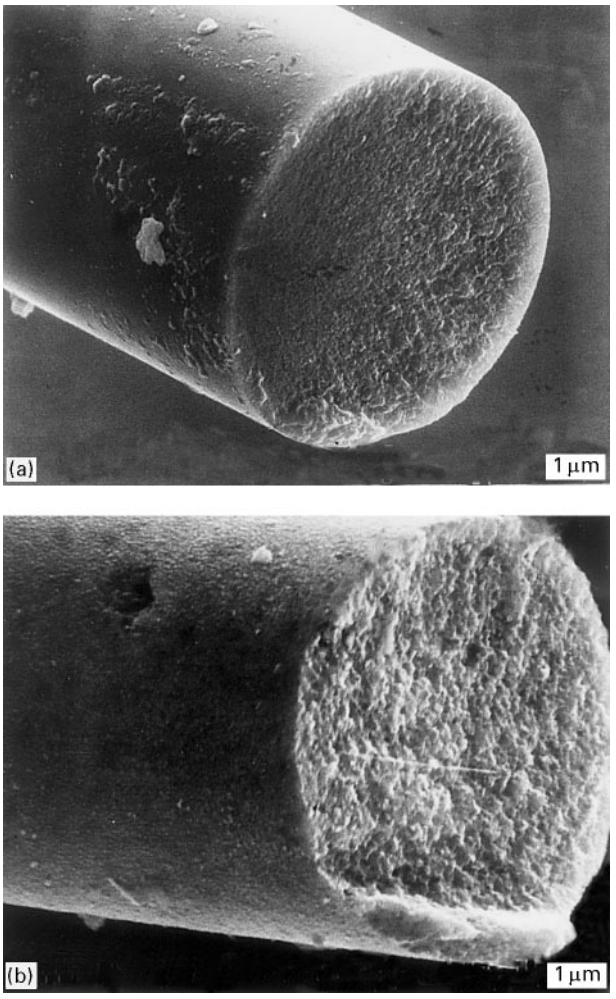

Figure 18 Fracture surfaces of Hi-Nicalon fibres annealed (a) 10 h at 1600 °C and (b) 1 h at 2000 °C and tested at room temperature.

T_p (≈ 30 nm for $T_p = 1600$ °C and $t_p = 1$ h) and with t_p (≈ 70 nm for $T_p = 1600$ °C and $t_p = 10$ h (Fig. 17).

3.2.2. Morphology

The morphology of heat-treated fibres remains unchanged up to 1600 °C for $t_p = 1$ h. For $t_p = 10$ h and $T_p = 1600$ °C, small crystals appear at the fibre surface and the failure surface becomes rougher (Fig. 18a), indicating that the fibre has undergone crystallization. The crystals are more abundant and larger at the fibre surface for $T_p = 1800$ °C and 2000 °C as well as apparently in the bulk (but at a much lesser extent) (Fig. 18b).

3.2.3. Microstructure

3.2.3.1. TEM analysis. At $T_p = 1400$ °C a SiC grain-growth is apparent from the SiC_{111} DF image (Fig. 19a) (with a maximum crystal size of 18–25 nm) and the SAD pattern (Fig. 20a). β-SiC is the prevalent structure, but polytypes are more frequently observed than in the as-received fibre. Additionally, joined crystals are occasionally observed (Fig. 20c). The free carbon is also better organized than in the as-received fibre (Fig. 20b). The number of aromatic stacked layers (N) is nearly the same as for the as-received

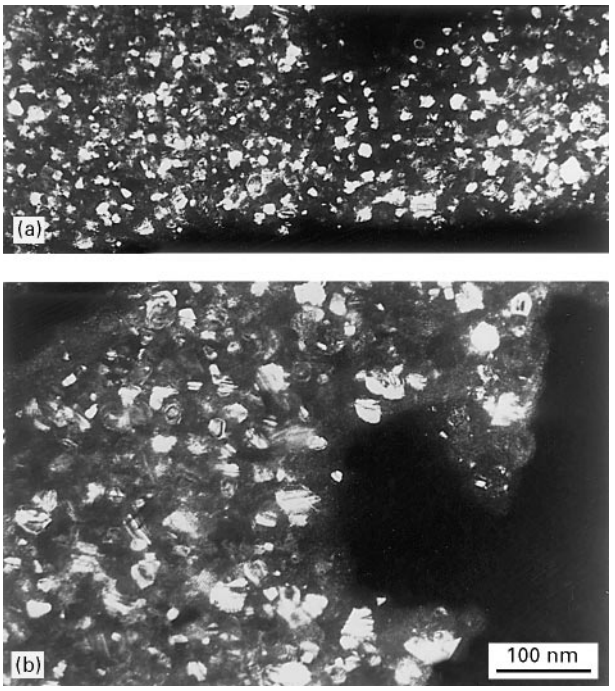

Figure 19 111-SiC dark field micrographs of heat-treated Hi-Nicalon fibres. 1 h at (a) $T_p = 1400\,^{\circ}C$ and (b) $T_p = 1600\,^{\circ}C$.

fibre, whereas the extent of the layers has slightly increased ($L_a = 3$–6 nm).

The three-dimensional texture of wrinkled carbon layers is more apparent than in the as-received fibre and still seems to form an incomplete network between SiC grains.

At $T_p = 1600\,^{\circ}C$ SiC grains as large as 50 nm are observed (Fig. 19b). The SAD pattern exhibits very punctuated SiC reflections and a considerable amount of evidence for stacking faults (Fig. 21a). Joined SiC-crystals are more apparent. The free carbon continues to organize with a higher average number of aromatic layers per stack (reaching $N = 7$–12) and more extended continuous aromatic domains ($L_a = 5$–10 nm) (Fig. 21b).

3.2.3.2. XRD analysis. Raising the annealing temperature results in a narrowing of the β-SiC reflections, assigned to crystal growth (Fig. 22). The average grain size (calculated from the Scherrer equation for the 111, 220 and 311 reflections) continuously increases for $1200 < T_p < 2000\,^{\circ}C$, reaching values of 10–12 nm for $T_p = 1600\,^{\circ}C$, and 20 nm for $T_p = 2000\,^{\circ}C$ (Fig. 23). A weak peak appears for $2\theta = 34.22^{\circ}$ ($d = 0.262$ nm) above $1200\,^{\circ}C$, as a shoulder on the 111 peak which becomes progressively separated as the temperature is raised.

3.2.3.3. Raman spectroscopy. The Raman spectroscopy data for the fibre bulk shows that increasing both T_p and t_p results in (i) a slight decrease of the relative intensity of the 1350 cm^{-1} band (normalized to the 1600 cm^{-1} band), (ii) a narrowing of the width of the two bands and (iii) a change in the shape of the 1600 cm^{-1} band, suggesting the occurrence of a doublet (Figs 24 and 25).

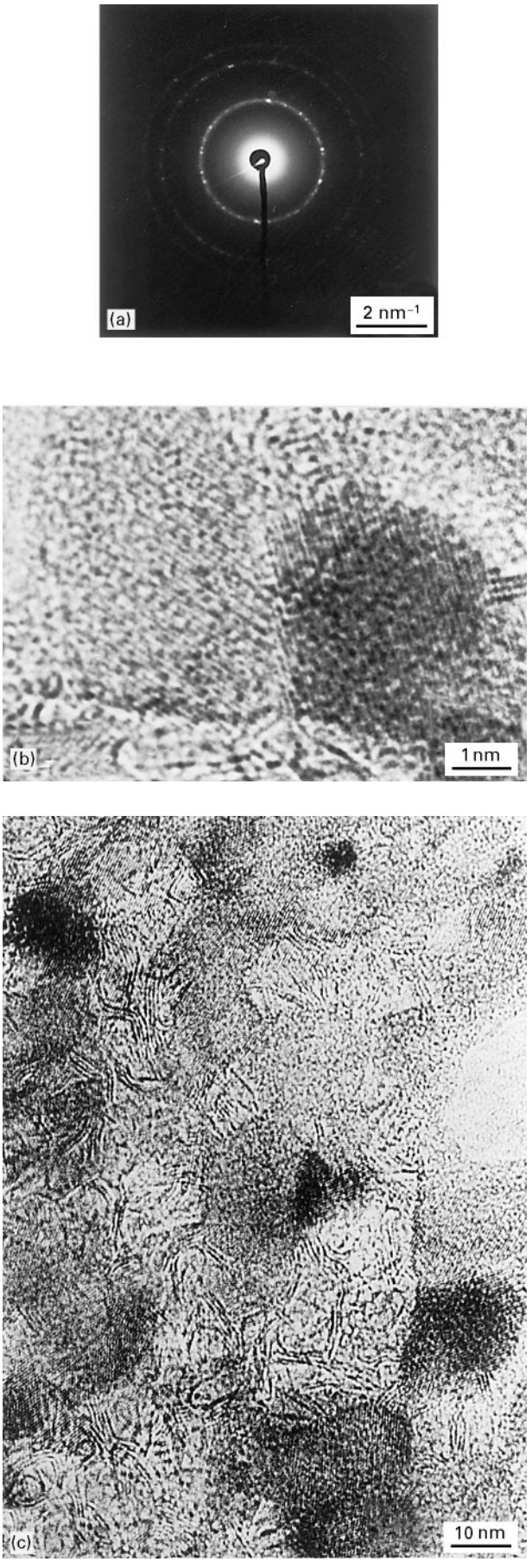

Figure 20 TEM micrographs of heat-treated Hi-Nicalon fibre (1 h at $T_p = 1400\,^{\circ}C$). (a) SAD pattern from the bulk, (b) HRTEM micrograph of Hi-Nicalon fibre heat-treated 1 h at $T_p = 1400\,^{\circ}C$ under pure argon and (c) enlargement HRTEM micrograph.

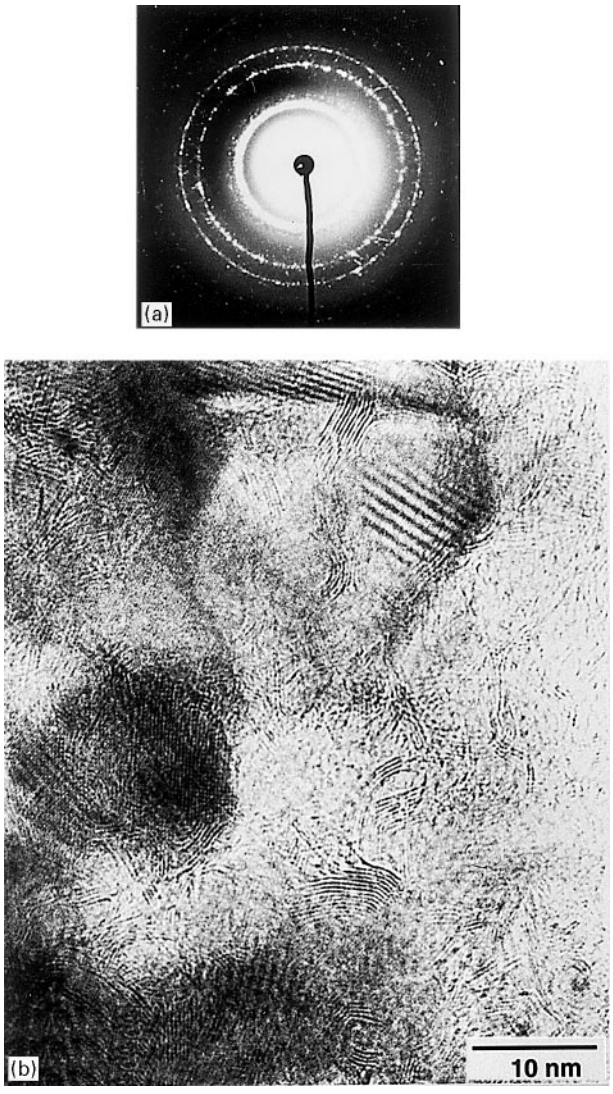

Figure 21 TEM micrographs of Hi-Nicalon fibre heat-treated 1 h at $T_p = 1600\,^{\circ}C$ under pure argon. (a) SAD pattern and (b) HRTEM micrograph of the bulk.

An analysis of the surface of the fibre ($T_p = 1600\,^{\circ}C$; $t_p = 10$ h) clearly shows that the relative intensity of the 1600 cm^{-1} peak and its width are respectively higher and lower than when measured in the bulk.

Beyond 1600 °C, a weak and narrow peak appears at 800 cm^{-1} whose intensity increases with t_p and when measured from the surface of the fibre. This peak is assigned to β-SiC [42–47].

3.2.3.4. Solid NMR analysis. No difference is observed between the as-received and the heat-treated fibre at a pyrolysis temperature of 1600 °C, for the ^{13}C MAS-NMR spectra except for a small change in the shape and a slight chemical shift towards a lower value of the peak centred at 130 ppm.

The −19 and −23 ppm components of the peak centred at −16 ppm on the ^{29}Si MAS-NMR spectra are slightly weaker after the heat treatment.

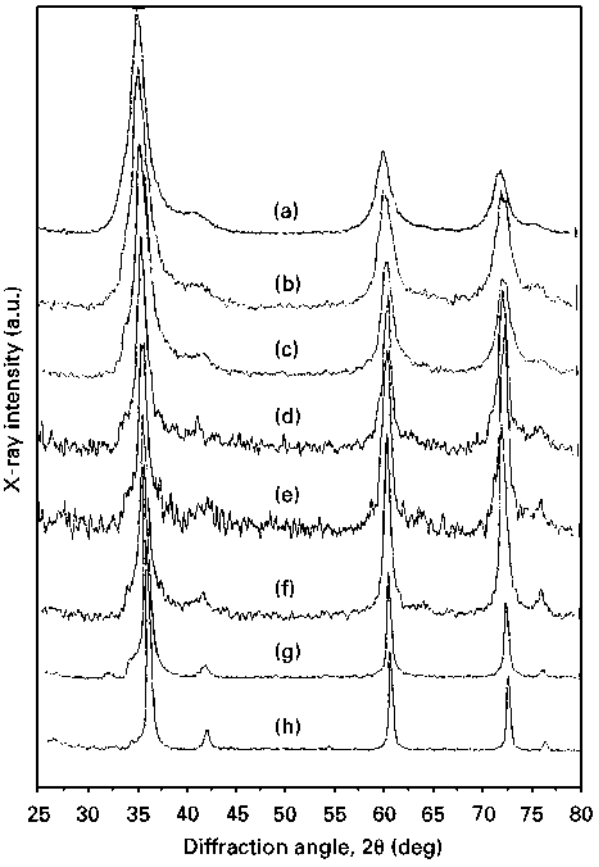

Figure 22 XRD spectra of Hi-Nicalon fibres, as a function of pyrolysis temperature (T_p) and duration (t_p), in argon (100 kPa). (a) As-received, (b) $T_p = 1200\,^{\circ}C$, $t_p = 1$ h; (c) $T_p = 1400\,^{\circ}C$, $t_p = 1$ h; (d) $T_p = 1500\,^{\circ}C$, $t_p = 1$ h; (e) $T_p = 1600\,^{\circ}C$, $t_p = 1$ h; (f) $T_p = 1600\,^{\circ}C$, $t_p = 10$ h; (g) $T_p = 1800\,^{\circ}C$, $t_p = 1$ h and (h) $T_p = 2000\,^{\circ}C$, $t_p = 1$ h.

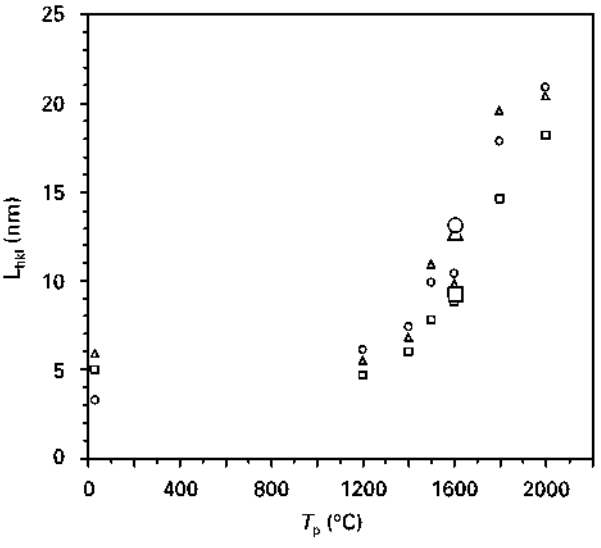

Figure 23 β-SiC crystalline apparent size of Hi-Nicalon fibres as a function of annealing temperature in pure argon (100 kPa). Data is presented for; (□) L111 (1 h), (△) L220 (1 h), (○) L311 (1 h), (□) L111 (10 h), (△) L220 (10 h) and (○) L311 (10 h).

3.2.4. Density

The density increases as the pyrolysis temperature is raised, from 1400–1800 °C (for $t_p = 1$ h) and as t_p is raised, from 1–10 h (for $T_p = 1600\,^{\circ}C$). It decreases beyond $T_p = 1800\,^{\circ}C$ (Fig. 26).

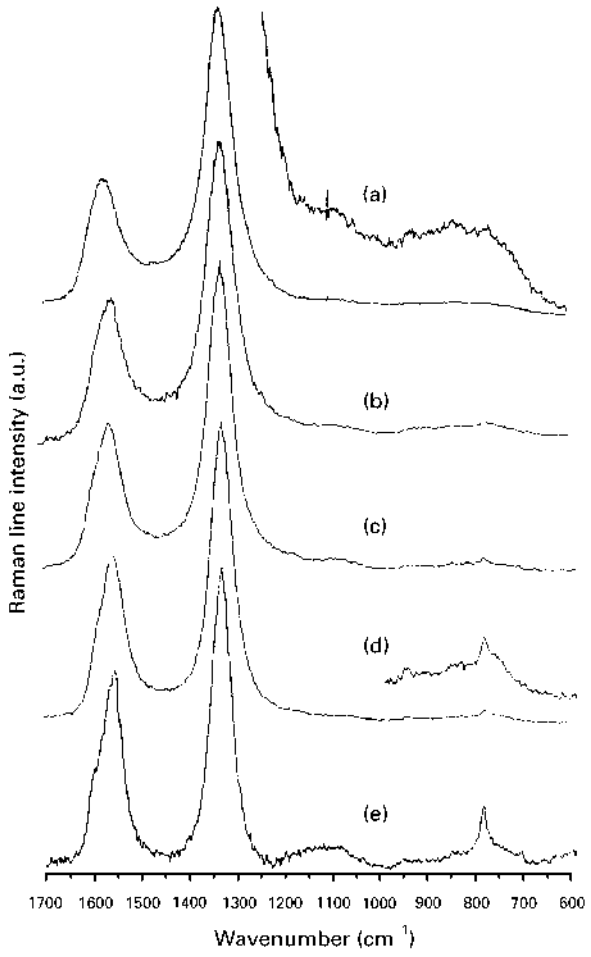

Figure 24 Raman spectra from the bulk and the surface of Hi-Nicalon fibres, as a function of pyrolysis temperature (T_p) and duration (t_p), in argon (100 kPa). (a) As-received (bulk), (b) $T_p = 1400\,^{\circ}C$, $t_p = 1$ h (bulk); (c) $T_p = 1600\,^{\circ}C$, $t_p = 1$ h (bulk); (d) $T_p = 1600\,^{\circ}C$, $t_p = 10$ h (bulk); (e) $T_p = 1600\,^{\circ}C$, $t_p = 10$ h (surface).

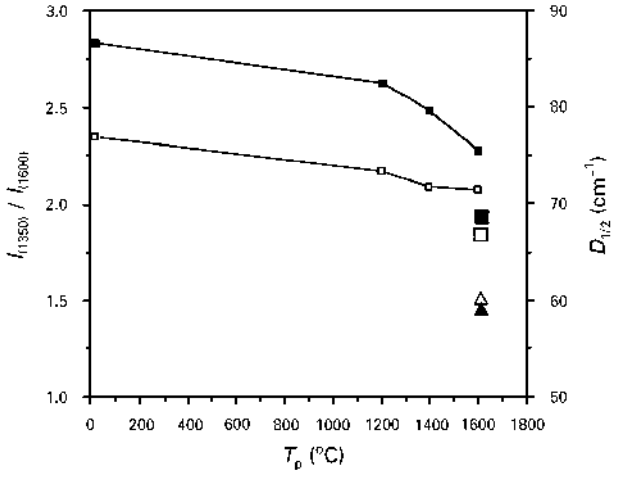

Figure 25 Variation of the $I_{(1350)}/I_{(1600)}$ ratio for samples annealed for (□) 1 h Ar, (□) 10 h Ar and (△) 10 h Ar (surface) and width at half height of the 1600 cm^{-1} Raman band for samples annealed for; (■) 1 h Ar, (■) 10 h Ar and (▲) 10 h Ar (surface) for Hi-Nicalon fibres.

3.2.5. TGA analysis under an inert atmosphere

The slight weight loss observed for the as-received fibre in the temperature range 1200–1400 °C is no longer observed when the fibre is pre-annealed

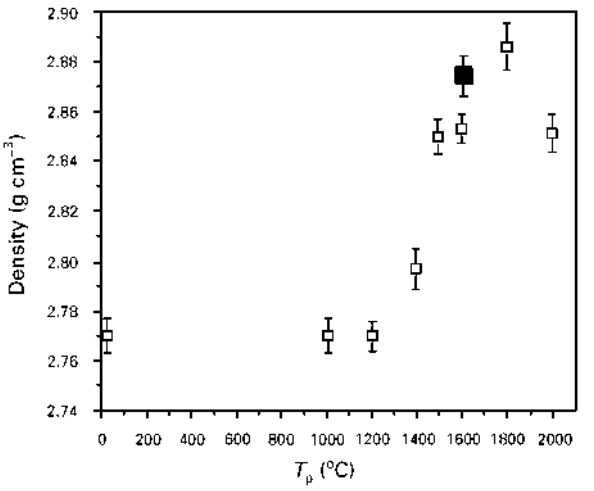

Figure 26 Density of Hi-Nicalon fibres as a function of annealing temperature (T_p) and duration; (□) $t_p = 1$ h, and (■) $t_p = 10$ h in argon (100 kPa).

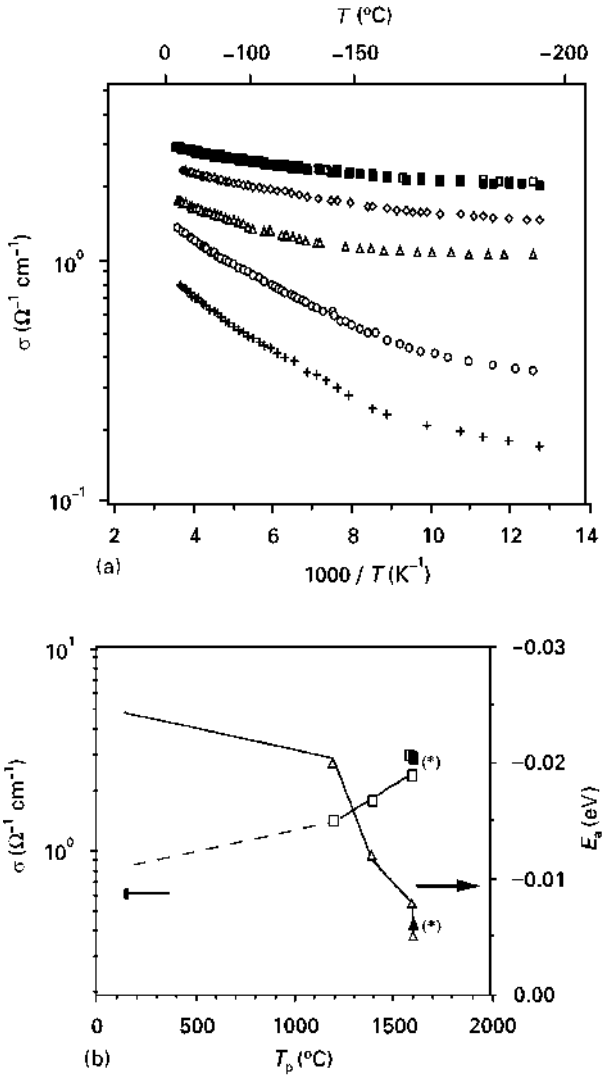

Figure 27 Electrical behaviour of Hi-Nicalon fibres: (a) thermal variations of the electrical conductivity data were collected at T_p values of (+) Fibre brute, (○) 1200 °C/1 h, (△) 1400 °C/1 h, (◇) 1600 °C/1 h, (□) 1600 °C/10 h and (■) 1600 °C/10 h and (b) (*Fibres intentionally oxidized after annealing at 1600 °C) variations of the electrical conductivity at ambient and apparent activation energy (determined in the range 200–300K), as a function of annealing temperature T_p.

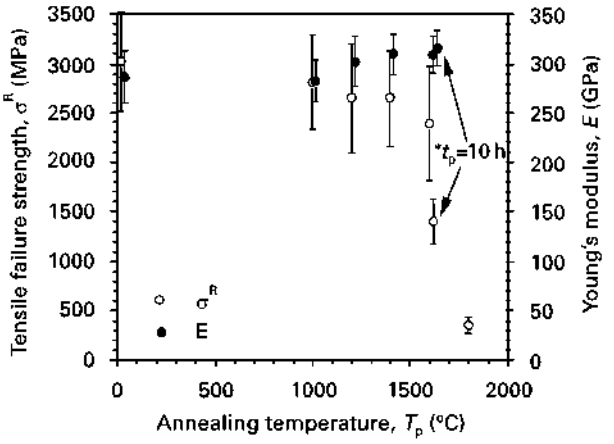

Figure 28 Variations of the tensile failure strength and Young's modulus at ambient of Si–C fibres, as a function of annealing temperature under argon (100 kPa) ($t_p = 1$ h except $^*t_p = 10$ h).

(1600 °C/1 h/Ar) (Fig. 9). No weight loss is detected until 1650 °C. However, a decomposition takes place beyond 1800 °C, as is the case for the untreated fibre.

3.2.6. Electron spin resonance

The g-value is almost unchanged when the fibre is heat-treated at $T_p = 1600$ °C, whilst the paramagnetic susceptibility (χ_p) and the spin concentration (N) both strongly decrease (Table II). Such a behaviour has already been observed for Si–C–O fibres, but at a lower HTT [48].

3.2.7. Electrical conductivity

The electrical conductivity (σ) measured at ambient increases with both T_p and t_p (Fig. 27), particularly in the range 1200–1400 °C. Furthermore, σ becomes continuously less temperature-dependant as the pyrolysis temperature is raised. The marked semiconducting behaviour of the as-received fibre vanishes as T_p is raised (i.e., the apparent activation energy decreases). The fibres annealed at 1600 °C (1 and 10 h) have been slightly oxidized (600 °C for 5 min) before the conductivity measurements in order to remove the thin carbon layer at their surface. Only a slight decrease of σ was observed after oxidation and no change in the electrical properties was detected, indicating that the electrical properties of the fibre depend on the bulk rather than on the surface carbon layer.

3.2.8. Mechanical properties at ambient

The tensile strength is almost unchanged for $T_p = 1400$ °C (Fig. 28). It decreases with T_p and t_p, initially only slightly (1400–1600 °C) and then dramatically. No important change in the Young's modulus is observed as T_p is raised.

4. Discussion

4.1. Thermal behaviour under an inert atmosphere

4.1.1. Chemical change

As expected, the oxygen free fibre has a much greater thermal stability from a chemical point of view as compared to its Si–C–O counterpart. In fact, the stability of the SiC + C mixtures is expected to be thermodynamically limited by the decomposition of SiC (reported to occur at about 2550 °C under a pressure of 1.013×10^5 Pa [50]). Conversely, that of the Si–C–O fibre is limited by the decomposition of the amorphous SiC_xO_y phase at temperatures in excess of $\approx$1200 °C [8–20]. Owing to the very low concentration of residual oxygen in the Si–C fibre, the oxycarbide phase is a minor constituent of the material. This feature is confirmed by the ^{29}Si MAS-NMR spectrum which shows the occurrence of only SiC_4 silicon sites (Fig. 8). Nevertheless, an oxygen-enriched layer is present at the surface of the as-received fibre. This layer is not thermally stable and decomposes at $T_p = 1200$ °C ($t_p = 1$ h) with the formation of $SiO_{(g)}$ and $CO_{(g)}$.

The fibre undergoes a slight superficial decomposition in the form of a silicon depletion. The carbon-enriched layer at the surface of the heat-treated fibres (as-observed by AES) does not result from a vapour deposition from the carbonaceous environment, since it was not observed on a pure SiC single crystal annealed in similar conditions. The carbon-enriched layer is detected at a temperature as low as 1400 °C at the fibre surface and progresses with increasing T_p and t_p through the bulk of the fibre. This carbon layer at the fibre surface could result from the decomposition of SiC nanocrystals (although it is expected to occur at a much higher temperature for the bulk polycrystalline SiC). A recent experimental study of the SiC + C system under vacuum at high temperatures has shown that gaseous silicon ($Si_{(g)}$) is the major species in the gas phase [50]. Under our annealing conditions and especially at the surface of the fibres, thermodynamic equilibrium might not be reached and thus, the evolution of $Si_{(g)}$ is expected to result in a silicon depletion of the surface of the fibres. This phenomenon could be strongly enhanced by the very small size of the SiC crystals (a few nm). Additionally, one might take into account the occurrence of an active oxidation mechanism, due to a very low residual oxygen pressure in the annealing furnace atmosphere or to residual oxygen within the fibre bulk. In that case, the decomposition would result locally in the evolution of silicon and carbon monoxides. $SiO_{(g)}$ is unstable at low temperature and is thought to condense onto the cool parts of the furnace or to react with the graphite crucible. Under these conditions, silicon monoxide would not reach its equilibrium pressure and thus a preferential evolution of $SiO_{(g)}$ with respect to $CO_{(g)}$ would be expected, resulting in a silicon depletion of the fibre.

4.1.2. Structural and textural changes

4.1.2.1. SiC phase. No structural evolution is detected below $T_p = 1200\,^{\circ}C$, suggesting that the fibre was fabricated at a temperature ranging from 1200–1400 °C. The SiC fibre is remarkably stable from a structural point of view at high temperatures with respect to the Si–C–O fibre. The oxycarbide phase, responsible for both chemical instability and drastic grain growth in the latter is almost non existent in the former. The thermal stability of the Si–C fibre is thus greatly improved and only a limited change in its microstructure is observed upon heating. Nevertheless, a slight β-SiC grain growth is still noticed at $T_p = 1400\,^{\circ}C$ in the bulk of the fibres in the TEM (Fig. 19) and XRD (Fig. 22) data. Since there is no change in the composition up to $T_p = 1800\,^{\circ}C$, the occurrence of a growth in the mean crystal size means that the two phases, (i.e., SiC and free carbon) segregate with increasing temperature (some SiC grains grow when others disappear). The driving force for this effect is the difference in surface or/and interface energy [51].

In the TEM data, SiC grains are often observed to be separated from each other by a free carbon intergranular phase, but they also might be connected through grain boundaries (although it is difficult to observe this by TEM). The diffusion of silicon-based species along the surface of SiC grains, and possibly also through the intergranular carbon phase, must be considered in order to explain the grain growth. This phenomenon would be helped by the high porosity of the intergranular material. If one assumes density values equal to $3.2\,g\,cm^{-3}$ for SiC and $1.8\,g\,cm^{-3}$ for free carbon, the overall porosity in the fibre should be 6%, or 25% in the pure intergranular phase. Atomic silicon might be the "feeding" species for SiC crystal growth, the carbon atoms being provided from the free carbon at the C/SiC interface. Owing to the presence of residual oxygen atoms (~1 at %), that are probably bonded to silicon atoms at the SiC grain surface at low temperature, silicon and carbon monoxides might also play a significant part in the SiC crystal growth, through a vapour-transport promoted mechanism. As a matter of fact, the total pressure at equilibrium on a $SiC + SiO_2 + C$ mixture of both $SiO_{(g)}$ and $CO_{(g)}$ species is about five orders of magnitude higher than that of $Si_{(g)}$ upon a SiC + C mixture at 1250 °C [50]. The bulk of the fibre can be considered as a closed system, since no chemical change is detected after heat-treatments of $T_p \leqslant 1800\,^{\circ}C$. These considerations suggest that the coarsening/shrinkage mechanism of the SiC crystals might also be promoted by a chemical transport of $SiO_{(g)}$ and $CO_{(g)}$ between the SiC grains, through the porous intergranular free carbon phase. The mechanism would be governed by the equilibrium equation:

$$2C_{(s)} + SiO_{(g)} \underset{(2)}{\overset{(1)}{\rightleftarrows}} SiC_{(s)} + CO_{(g)} \qquad (4)$$

with $\log(P_{SiO}/P_{CO}) = -2.26$ at 1800 K [52]), Equation $4_{(1)}$ being responsible for the grain growth of SiC crystals and Equation $4_{(2)}$ for their shrinkage. It is well known that an exaggerated grain growth during sintering (which is detrimental to densification) of an oxygen-containing SiC powder (≈ 0.5 wt %) is related to vapour transport by SiO [53, 54].

The SiC grain shrinkage in the fibre is expected to also result in free-carbon formation. The uncompleted carbon cages around SiC crystals which are increasingly observed by TEM analysis as T_p is raised (Figs 20 and 21), could be partly due to such a phenomenon especially at a high annealing temperature. This assumption seems to be confirmed by the fact that at $T_p = 1600\,^{\circ}C$, thick and curved carbon layer stacks are observed around small size SiC crystals (or even pores) rather than around the larger-size crystals.

Such a mechanism of crystal growth is very different from that occurring during the Si–C–O fibre degradation. The former takes place under near chemical-equilibrium conditions and is driven by the lowering of surface energy, while the latter takes place far from equilibrium, as a result of chemical reactions involving the metastable $SiO_xC_{(1-x/2)}$:

$$SiO_xC_{(1-\frac{x}{2})} \rightarrow SiO_{(g)} + (x-1)\,CO_{(g)} + \left(2 - \frac{3x}{2}\right)C_{(s)} \qquad (5)$$

$$SiO_{(g)} + 2C_{(s)} \rightarrow SiC_{(s)} + CO_{(g)} \qquad (4_1)$$

For very high temperatures, $T_p > 1800\,^{\circ}C$, a silicon depletion is observed mainly at the surface of the low-oxygen fibres (but it also occurs in the core), owing to the decomposition of SiC. In addition to that phenomenon, β-SiC crystals with a large size (a few μm) are observed at the surface of the fibres. These grains are partly inlayed in the fibre, suggesting the growth mechanism depicted in Equation 4. However, since the main part of the grain is free, a vapour–vapour induced reaction is thought to be more likely as the coarsening mechanism. If traces of oxygen still remain in the atmosphere then the following reaction may be involved:

$$SiO_{(g)} + 3CO_{(g)} \rightarrow SiC_{(s)} + 2CO_{2(g)} \qquad (6)$$

followed by the CO_2 reduction and oxidation of the free carbon of the fibre or of the graphite crucible according to:

$$CO_{2(g)} + C_{(s)} \rightarrow 2CO_{(g)} \qquad (7)$$

Equations 6 and 7 represent the overall reaction:

$$SiO_{(g)} + 2C_{(s)} \rightarrow SiC_{(s)} + CO_{(g)} \qquad (4_1)$$

These reactions can be used to explain the SiC crystal growth, in terms of a mechanism involved in the SiC whiskers growth [55]. Shimoo *et al.* have also noticed such a large crystal growth on the skin of low oxygen SiC fibres, but after treatments at a lower heat-treatment temperature (from $T_p > 1600\,^{\circ}C$) [56]. A higher residual oxygen pressure in the annealing atmosphere might be responsible for this phenomenon (alumina environment).

Such large crystals are not observed within the bulk of the fibre, due to the presence of the free carbon phase which inhibits the grain-boundary and/or

gaseous diffusion, required for recrystallization. Furthermore, a carbon excess induces a lowering of the $SiO_{(g)}$ pressure thereby inhibiting the vapour-transport reactions (Equation 4) responsible for the grain-coarsening [53, 54].

The occurrence of SiC polytypes in addition to the β-SiC phase in the fibre can be assessed by the MAS-NMR and TEM analyses. In fact, both characteristic peaks of the SiC_4 and CSi_4 sites on the ^{29}Si and ^{13}C MAS-NMR spectra can be decomposed into 2 or 3 components (Fig. 8). This unexpected feature (under the assumption of a pure β-SiC phase) suggests the presence of additional SiC polytypes [57], which is in agreement with other studies on the pyrolysis of PCS [58]. This assumption is also confirmed in the XRD data by the existence of a shoulder on the SiC-111 peak ($2\theta = 34.22^\circ$, $d = 0.262$ nm) (Fig. 6), which is absent in a pure β-SiC pattern, and which becomes continuously better defined for the Hi-Nicalon fibres, as T_p is raised. Stacking faults (with respect to β-SiC) are also observed by TEM but the presence of any other crystalline SiC phases has not been formally confirmed. The slight decrease of the -19 and -23 ppm components with regard to the peak centred at -16 ppm (SiC_4) on the ^{29}Si MAS-NMR spectra, suggests that stacking faults tend to decrease within the β-SiC structure after a 1600 °C heat treatment.

4.1.2.2. Free carbon phase. The texture of the free carbon phase in the Si–C fibre, is also very different from that of the Si–C–O fibre. The molar fractions are almost the same (respectively 30 and 28 mol %) but the material is apparently better organized in the Si–C fibre, in the form of a discontinuous network between the SiC crystals. In the Si–C–O fibre, free carbon was present as a basic structural unit (BSU) still partly hydrogenated (i.e., 2–3 stacked aromatic layers of about 12 rings) surrounded by a continuous $SiO_xC_{(1-x/2)}$ phase ($0 \leqslant x \leqslant 2$) [7, 42]. In the Hi-Nicalon fibre, most of the hydrogen atoms have been eliminated from the material during the fibre pyrolysis. In fact, ERDA indicates a very low residual hydrogen content. Furthermore, neutron diffraction (which is very sensitive to hydrogen), has not shown the presence of any hydrogen in the as-received fibre. Residual hydrogen has been shown to exist in pyrolysed PCS in significant amounts for $T_p = 1200$ °C (≈ 5 at % from NMR analysis) but its concentration decreases strongly at higher temperatures (to ≈ 0.6 at % at 1400 °C) [59]. Hydrogen is usually assumed to be bonded to the free carbon phase, at the periphery of the aromatic layers [5, 7, 36]. Our data suggest that the hydrogen atoms bonded to carbon atoms at the periphery of the carbon layers were eliminated during the carbonization of PCS in the Hi-Nicalon fibres. It is known that, for carbon materials, the removal of hydrogen is strongly related to an increase in the number of free radicals [60]. In fact, a large number of paramagnetic centres (ESR data) are present in the as-received fibre, which are assigned to the free carbon phase. They are thought to result from the rupture of C–H side-bonds in the carbonaceous phase. The spin concentration for Hi-Nicalon fibre is very high with respect to other carbonaceous materials, especially considering that the free carbon phase accounts for only about 11 wt % of the whole material. When the annealing temperature is raised, the growth of the carbon layers corresponds to a decrease of localized spin centres [48, 60].

Heat-treatment of the fibre at increasing temperatures results in a gradual organization of the free carbon phase in terms of the size of the carbon layers (L_a) and the number of stacked layers (N) or the thickness of the stacks L_c.

After an annealing treatment performed at $T_p = 1400$ °C, from the LF TEM images (Figs 5 and 20), the carbon domains are apparently slightly larger than in the as-received fibre ($L_a = 3$–6 nm and 2–3 nm respectively, with no significant change in N). This organization of the free carbon phase might be explained (i) by the dewrinkling of the aromatic layer stacks and/or (ii) edge to edge association producing longer distorted layers. Despite the very low hydrogen concentration of the fibre, the arrangement of the carbon phase apparently corresponds to a simultaneous slight hydrogen evolution from the material (as assessed by ERDA) resulting from the rupture of the residual C–H bonds.

For $T_p = 1600$ °C, the organization of the carbon network is further improved. The free-radical concentration decreases due to condensation and consequent extension of the carbon domains. The size of the wrinkled aromatic layers slightly increases ($L_a = 5$–10 nm) in addition to the number of aromatic layers within the stacks ($N = 7$–12 versus $N = 5$–8 for the as-received or 1400 °C-annealed fibre). Furthermore, the carbon layer stacks tend to organize flat on the surface of the SiC crystals. This behaviour has been observed for pyrolysed PCS [42] and also during the thermal degradation of carbides where the decomposed crystals are coated with aromatic layers stacked flat upon their surface, forming perfect shells [61].

It is noteworthy that the organization process of the carbon phase in Hi-Nicalon is somewhat different from that usually reported for non graphite forming carbons resulting from the pyrolysis of an organic precursor, according to which a growth in N or L_c is observed first (stages 2 and 3 from [61]). This feature might be explained by the fact that the organization of the carbon phase takes place within a confined space limited by SiC-crystal faces (the major phase) in which, additionally, transport phenomena via the gas phase might occur.

Heat treatments at increasing temperatures (T_p) result in a moderate densification of the fibre, which starts between 1200–1400 °C and becomes significant for $T_p = 1500$ and 1600 °C. This feature corresponds to the temperature beyond which the first structural changes are observed, and suggests that the fibres were prepared at 1200–1400 °C. This densification cannot be assigned to the SiC phase since it is already highly crystallized in the as-received fibre. The component responsible for the density increase seems to be the intergranular porous material and especially the free carbon rather than SiC. The densification is related to the progressive organization of free carbon discussed

above associated to a collapse of pores. For $T_p = 1600\,^{\circ}C$, the density of the fibre is still lower than its theoretical value (2.97 $g\,cm^{-3}$ for a fully crystallized material) owing to the turbostratic nature of the carbon phase, whose density is lower than that of graphite.

From the literature, during the formation of graphite from poorly crystallized carbon the main features of the corresponding Raman spectra are: (i) a decrease of the width of the two peaks at 1350 and 1600 cm^{-1}, (ii) an increase of their intensity ratio (I_{1600}/I_{1350}) and (iii) a shift of the E_{2g} peak from 1600 to 1580 cm^{-1} (in fact this peak is a doublet: the intensity of the 1600 cm^{-1} component decreases, as the reaction proceeds and the two peaks continuously separate). These features have been observed to be directly related to the organization and crystallization of the carbon structure and texture [39–43]. A quantitative relationship between the I_{1600}/I_{1350} ratio and the graphite crystal size has also been established and validated by XRD analysis [40].

The Raman spectra of the Si–C and the Si–C–O fibres contain inconsistent features: as-expected, the vibration bands of the spectrum of the Si–C fibre are sharper than those for the Si–C–O fibres, due to the better organization state of the free carbon phase. Conversely, the I_{1600}/I_{1350} ratio is unexpectedly low for the Si–C fibre. This phenomenon is not yet understood. It might be related to the different microstructures of the carbon phases in the two types of fibre as discussed previously.

The spectra of the fibre at increasing T_p (Fig. 24) illustrate the progressive organization of the carbon already observed by TEM which results in (i) a slow decrease in intensity of the 1350 cm^{-1} peak, (ii) a more pronounced decrease of the E_{2g} peak width and (iii) some splitting of the doublets at 1580–1600 cm^{-1} whose 1580 cm^{-1} component intensity increases. A third peak at 800 cm^{-1} assigned to silicon carbide clearly appears for $T_p \geqslant 1400\,^{\circ}C$ whose intensity increases with T_p, owing to the coarsening of β-SiC.

4.1.3. Changes in the electrical properties

It appears from the measurements on the as-received Hi-Nicalon fibre ($\sigma \approx 1\ \Omega^{-1}\,cm^{-1}$ at ambient) that the component controlling the electrical behaviour is obviously the free-carbon rather than the β-SiC phase. In fact, σ currently ranges from 1–100 $\Omega^{-1}\,cm^{-1}$ for nanocrystalline carbons resulting from the carbonization of aromatic hydrocarbons [41, 60], whilst it is only about $10^{-5}\ \Omega^{-1}\,cm^{-1}$ for polycrystalline SiC, at ambient.

The as-received fibre exhibits a semi-conducting behaviour. This feature is also commonly encountered in carbon materials. Such a behaviour can not be explained by a classical crystalline semi-conducting model (graphite behaves as a semi-metal), but rather by the Mott-CFO model (from Cohen, Frische and Ovshinsky), which involves an apparent semi-conducting behaviour with an apparent activation energy (as determined from σ measurements), for amorphous or partially organized materials [60]. Non-crystalline carbons can be described as a mixture of two phases; the former is made of stacked carbon layers, long enough to be conductive, whereas the latter is insulating (poorly organized carbon, pores, spacing between the hydrogenated periphery of aromatic domains). The "coalescence" of the conductive domains, observed during the heat-treatments at increasing temperature, gives rise to a fast increase in conductivity according to a percolation effect [60].

On the basis of the variations of the electrical behaviour of carbon materials as a function of the heat-treatment temperature and of the previously described structural and textural changes in the fibre, the electrical properties of the fibre can be discussed as follows:

The electrical conductivity (σ) increases after a heat treatment at a temperature as low as 1200 °C, whilst no apparent chemical or structural changes were observed (Fig. 27). This feature might be related to a small release of residual hydrogen, although the fibre is thought to have been prepared at a higher temperature. When the remaining hydrogen atoms, located at the boundary of the carbon domains (at the periphery of the aromatic layers) are released, the mobility of the free charge carriers through the intergranular carbon phase is improved according to the mechanism described above. This does not necessarily result in an apparent organization of the texture of the free carbon.

The conductivity continues to increase and the apparent activation energy decreases between 1200–1400 °C, probably as a result of the organization of the free carbon phase (as observed by TEM and RSMA). From a structural point of view, these features result in (i) a collapse of pores and a densification and (ii) in an increase of the size of the conductive carbon domains, in agreement with the percolation effect reported for carbon materials.

For $T_p = 1600\,^{\circ}C$ ($t_p = 1$ h) σ still increases as the carbon crystallites grow slightly in length and thickness. An evolution of σ is also noticed for increasing the annealing time ($t_p = 10$ h) and it becomes nearly temperature independent similar to graphite materials.

4.1.4. Mechanical changes

The thermal stability of the PCS-derived fibre is greatly improved by the use of an oxygen-free curing process, both from a chemical and structural point of view. In fact, the failure strength (σ^R) at room temperature of the fibres is unchanged for $T_p \leqslant 1400\,^{\circ}C$, and a slight decrease is only noticed ($\approx 15\%$) after a 1600 °C/1 h annealing treatment. As a comparison, the failure strength of Si–C–O fibres drops after annealing at temperatures as low as 1200 °C for $t_p = 1$ h, or even 1000 °C for $t_p = 10$ h, owing to the decomposition of the SiO_xC_y phase [13–16].

Despite the low oxygen content of the Si–C fibre a decomposition takes place at the fibre surface, resulting in a silicon depleted layer and SiC crystal growth. These features are thought to induce the formation of surface flaws of large size and thus, a decrease of σ^R. The Young's modulus of the as-received Si–C fibre is much higher than that of the Si–C–O

fibres (285 GPa versus 200 GPa). This correlates with the fact that (i) the fibre contains larger amounts of better organized crystalline phases (SiC and free-carbon) and (ii) the compliant SiC_xO_y amorphous phase is almost no longer present in the Si–C fibre. Only a small change in E is observed after annealing at increasing T_p. A slight increase for $T_p \geqslant 1200\,^{\circ}C$ could be assigned to the densification of the fibre.

4.2. Thermal behaviour under an oxidizing atmosphere

The oxidation behaviour of silicon-based materials has been widely studied for many years [62–74]. They are characterized by a good oxidation resistance under high oxygen pressures owing to the formation of viscous silica at the surface of the material which limits the oxygen diffusion. Within the passive regime, the kinetics of growth of the oxide layer are usually reported to obey a parabolic law. Such a time dependence indicates that, similar to pure silicon [62], the oxidation of SiC is controlled by molecular-oxygen diffusion through the growing silica layer [75]. Oxidation kinetics are subjected to large variations, and, unexpectedly, to highly variable thermal dependences (activation energies currently ranging from 80 –500 kJ mol^{-1}). This discrepancy is thought to be related to the different nature of the studied materials (single crystals or polycrystalline (CVD or sintered) SiC).

Only a few authors have investigated the oxidation kinetics of SiC fibres, in air or dry oxygen [69–74]. Filipuzzi and Naslain [71] and also Shimoo *et al.* [72] established from TGA experiments that a parabolic law is obeyed for the oxidation of Si–C–O fibres within the temperature range of 800–1200 °C. Beyond 1200 °C, the crystallization temperature of the oxide film, the formation of microcracks and the thermal metastability of the Si–C–O fibres enhance the oxidation kinetics. Activation energies derived from parabolic kinetic constants are lower (70–80 kJ mol^{-1} [71] or 137 kJ mol^{-1} [74]) than those generally reported for pure SiC. This behaviour could be related to the diffusion of residual hydrogen from the bulk of the fibre, through the silica scale and/or to the formation of a porous oxide [71].

The oxide film remains smooth, apparently crack-free and adhesive for $1000 \leqslant T \leqslant 1400\,^{\circ}C$ (Fig. 13). The thickness of the silica is constant along the fibre (when $e \leqslant 1\,\mu m$) indicating that oxidation was not locally favoured by flaws, from the fibre or within the oxide layer (bubbles, cracks).

At 1000 °C, the silica is amorphous. Crystallization starts at 1200 °C and mainly yields α-cristobalite. The crystallization of silica is generally reported to occur at a temperature close to 1400 °C [64]. Such unexpected behaviour at a temperature as low as 1200 °C, might be related to the presence of traces of Al, Ca, Na, Mg in ex-PCS fibres [10], which are known to enhance crystallization [64, 65] and are also reported to increase the oxidation rate [66, 67]. The volume change and viscosity loss occurring during the transition apparently do not affect the protective barrier to oxygen diffusion of the oxide film for $T \leqslant 1400\,^{\circ}C$ and $t \leqslant 15$ h (Fig. 13b).

An increase of the volume of oxidized filaments is noticed during the growth of the silica. The product (silica) to reactant volume ratio (Δ) is equal to 1.66, indicating that the expanding oxide scale has the capability of covering the substrate in a continuous manner. Despite crystallization, the oxide layer is thought to be viscous enough at 1400 °C, to release mechanical stresses and thus, to maintain a protective covering.

This is apparently no longer true for $T > 1400\,^{\circ}C$ (Fig. 14). The silica thickness is much higher (reaching few μm) and comprises several debonded concentric layers. The texture of the oxide layer is thought to have been formed at high temperatures rather than during the fast cooling (irregular cracks would have been visible). The oxidation kinetics are probably too fast and the viscosity of the oxide, enhanced by crystallization, too high for the stresses induced by the volume change to be released.

The growth kinetics of the silica layer on the Si–C filaments in dry oxygen obey a parabolic law in the temperature range 1000–1400 °C for $t \leqslant 15$ h (Fig. 12) and the kinetic constants (K_T) are close to those obtained for the oxygen-cured fibre, within the range 1000–1200 °C [71]. One should notice that a parabolic law is still obeyed up to 1400 °C for the Si–C fibre, whereas this is no longer true beyond 1200 °C for the Si–C–O Nicalon fibre [71, 72]. This feature is related to the higher thermal stability of the oxygen-free fibres.

A parabolic law is ruled-out for $T > 1400\,^{\circ}C$ or is only observed for a short period ($t < 2$–3 h) at $T = 1500\,^{\circ}C$. The kinetics of growth of the oxide layer become apparently linear for $T = 1500\,^{\circ}C$ and $t > 3$ h, suggesting that the layer is no longer protective. This feature correlates with the formation of a discontinuous and unprotective oxide layer as a consequence of the stresses induced by the volume changes during the oxidation of the ceramic and the crystallization of the silica layer. Oxygen diffusion is made easier and therefore, dramatically enhances the oxidation rate.

Oxidation kinetics are thermally activated (Equation 3), for various Si-based materials. Equation 3 is obeyed within the 1000–1400 °C temperature range (Fig. 15). The apparent activation energy ($E_a = 107 \pm 4$ kJ mol^{-1}) is lower than that reported by Shimoo *et al.* for a similar material (234 kJ mol^{-1} [74]), but is similar to those found for Si–C–O fibres (80–137 kJ mol^{-1} [71, 72]) or pure silicon (117 kJ mol^{-1} [62]).

This E_a value suggests that the oxidation mechanism for low oxygen Si–C fibres within the temperature range 1000–1400 °C, is also controlled by permeation of molecular oxygen through the growing oxide film ($E_a = 113$ kJ mol^{-1}). Nevertheless, the kinetic constants at a given temperature, are higher, and the E_a values are much lower for the Si–C fibres than those reported for pure polycrystalline SiC (150–300 kJ mol^{-1}). The oxidation behaviour of the latter is complicated by the presence of dopants (sintering aids) and the propensity for crystallization of

the oxide film. Costello and Tressler found E_a values as low as 120 kJ mol^{-1} for the oxidation of (0001) Si face in a SiC single crystal (the crystal face exhibiting the highest oxidation rate) and 140 kJ mol^{-1} for thermally deposited SiC (CNTD) [65]. These oxidation data are very similar to those observed for the Si–C fibres.

5. Conclusion

Oxygen-free fibres (< 1 at %) prepared according to a spinning/electron-beam curing/pyrolysis process consist of a mixture of β-SiC nanocrystals of about 5 nm in average size (2–15 nm) and free carbon. The carbon phase consists of stacked carbon layers, 2–3 nm in extension (L_a) with ≈ 5 layers by stack. (7–8 layers are also observed). The carbn stacks are aggregated edge-to-edge between the SiC crystals, where they usually lie flat on their faces, building a carbon network along the fibre.

With respect to the Si–C–O fibre, this microstructure gives rise to original properties such as improved density (2.77 versus 2.56 g cm^{-3}), stiffness (285 versus 200 GPa) and electrical conductivity (≈ 1 versus $10^{-4}\ \Omega^{-1}\cdot cm^{-1}$). The Si–C fibres clearly show a much greater thermal stability due to the absence of the unstable SiO_xC_y phase.

However, despite the chemical stability of the fibre, a slight structural evolution of both SiC and free carbon occurs within $T_p = 1200$–$1400\,^{\circ}C$ and improves with increasing t_p and T_p. Residual oxygen is thought to be partly responsible for the β-SiC grain growth through the formation of silicon and carbon monoxide species. As T_p is raised, a β-SiC grain growth is observed. Simultaneously, the small carbon layer stacks are observed to organize into larger distorted domains ($T_p \geqslant 1400\,^{\circ}C$) and along the *c*-axis, into thicker stacks at higher temperatures ($T_p \geqslant 1600\,^{\circ}C$).

A moderate decomposition is also observed beyond $T_p = 1400\,^{\circ}C$ at the fibre surface, in the form of a carbon enriched layer. This layer which is observed to increase in thickness with t_p and T_p could be related to an active oxidation mechanism, involving an evolution of silicon and carbon monoxides. This phenomenon might be responsible for the formation of surface flaws and the strength decrease of the fibres observed beyond $T_p = 1600\,^{\circ}C$.

The Si–C fibres have almost the same oxidation resistance as the Si–C–O fibres but a parabolic growth law for the silica thickness is obeyed up to 1400 °C for the former, whereas it is no longer true beyond 1200 °C for the latter. For $T_p = 1500\,^{\circ}C$, the silica no longer protects the fibre and a parabolic law is no longer valid.

Appendix: Calculation of the silica layer thickness of oxidized filaments from TGA data

(I) Definition of coefficients and data relating to as-received and oxidized fibres

(a) *Silica coefficients*

Let M_{Si} and M_{SiO_2} be the silicon and silica molar masses, and d_{SiO_2}, the silica density, respectively.

(b) *As-received fibre data*

Let m_0, r_0, d and C_{Si} be the starting mass, average radius, density and silicon mass concentration of the as-received fibre.

(c) *Oxidized fibre data*

Let Δm, r_e, r_i and e be the mass variation, the external radius, the radius of the non-oxidized core of the fibre and the silica thickness.

(II) Calculation of the silica layer thickness

The relative mass variation is defined according to the equation:

$$\frac{\Delta m}{m_0} = \left(\frac{r_i}{r_0}\right)^2 \cdot \left(1 - \frac{d_{SiO_2}}{d}\right) + \left(\frac{r_e}{r_0}\right)^2 \cdot \frac{d_{SiO_2}}{d} - 1 \tag{A1}$$

furthermore, the silicon mass into the oxidized fibre is equal to that into the formed silica. Then

$$\pi \cdot C_{Si} \cdot (r_0^2 - r_i^2) \cdot d = \pi \cdot \frac{M_{Si}}{M_{SiO_2}} \cdot (r_e^2 - r_i^2) \cdot d_{SiO_2}$$

or:

$$C_{Si} - \frac{M_{Si}}{M_{SiO_2}} \cdot \frac{d_{SiO_2}}{d} \cdot \left(\frac{r_e}{r_0}\right)^2 + \left(\frac{M_{Si}}{M_{SiO_2}} \cdot \frac{d_{SiO_2}}{d} - C_{Si}\right) \cdot \left(\frac{r_i}{r_0}\right)^2 = 0 \tag{A2}$$

If A and Δ are defined by

$$A = C_{Si} \cdot \frac{M_{SiO_2}}{M_{Si}} \text{ and } \Delta = A \cdot \frac{d}{d_{SiO_2}}$$

(Δ being the Pilling–Bedworth factor i.e., the volume ratio of formed silica and oxidized material), r_e and r_i can be inferred from Equations (A1) and (A2). Then

$$\left(\frac{r_i}{r_0}\right)^2 = 1 + \frac{1}{(1-A)} \cdot \frac{\Delta m}{m_0}$$

$$\left(\frac{r_e}{r_0}\right)^2 = 1 + \frac{(1-\Delta)}{(1-A)} \cdot \frac{\Delta m}{m_0}$$

and finally:

$$e = r_e - r_i$$

Note that for low $\Delta m/m_0$ values, e can easily be written as

$$e \approx \frac{1}{2} \cdot r_0 \cdot \frac{\Delta}{A-1} \cdot \frac{\Delta m}{m_0}$$

or

$$e \approx \frac{1}{2} \cdot r_0 \cdot \frac{M_{SiO_2} \cdot C_{Si}}{M_{SiO_2} \cdot C_{Si} - M_{Si}} \cdot \frac{d}{d_{SiO_2}} \cdot \frac{\Delta m}{m_0}$$

Acknowledgements

This work was supported by SEP and CNRS. The authors are indebted to Nippon Carbon for the supply of the Hi-Nicalon samples. They gratefully thank Pr. Legrand from Laboratoire de Physique Quantique (ESPCI, Paris) for the NMR analyses, Pr. Delhaes, Pr. Marchand, M. Amiell and Dr. Canet from Centre de Recherche Paul Pascal (UPR from CNRS, Pessac) for the ESR analyses and their assistance in the

conductivity measurements, Dr. Couzi from Laboratoire de Spectroscopie Moléculaire et Cristalline (URA from CNRS, Talence) for the Raman analyses and H. Guegan, from Centre d'Etudes Nucléaires de Bordeaux Gradignan, for providing ERDA results.

References

1. S. YAJIMA, J. HAYASHI and M. OMORI, *Chem. Lett.* **9** (1975) 931.
2. S. YAJIMA, K. OKAMURA and M. OMORI, *ibid.* **12** (1975) 1209.
3. S. YAJIMA, K. OKAMURA, J. HAYASHI and M. OMORI, *J. Amer. Ceram. Soc. Bull.* **59** (1976) 324.
4. S. YAJIMA Y. HESEGAWA J. HAYASHI and M. IIMURA, *J. Mater. Sci.* **13** (1978) 2529.
5. C. LAFFON, A. M. FLANCK, P. LAGARDE, M. LARIDJANI, R. HAGEGE, P. OLRY, J. COTTERET, J. DIXMIER, J. L. MIQUEL, H. HAMMEL and A. P. LEGRAND, *ibid.* **24** (1989) 1503.
6. L. PORTE and A. SARTRE, *ibid.* **24** (1989) 271.
7. P. LE COUSTUMER, M. MONTHIOUX and A. OBERLIN, *J. Eur. Ceram. Soc.* **11** (1993) 95.
8. T. MAH, N. LECHT, D. E. Mc CULLUM, J. R. HOENIGMAN, H. M. KIM, A. P. KATZ and H. A. LIPSITT, *J. Mater. Sci.* **19** (1984) 1191.
9. T. J. CLARK, R. M. ARONS, I. B. STAMATOFF and J. RABE, *Ceram. Engng. and Sci. Proc.* **6** (1985) 576.
10. S. M. JOHNSON, R. D. BRITTAIN, R. H. LAMOREAU and D. J. ROWCLIFFE, *J. Amer. Ceram. Soc.* **71** (1988) C-132.
11. P. SCHRECK, C. VIX-GUTERL, P. EHRBURGER and J. LAHAYE, *J. Mater. Sci.* **27** (1992) 4237.
12. T. SHIMOO, H. CHEN and K. OKAMURA, *J. Ceram. Soc. Jpn.* **100** (1992) 48.
13. T. J. CLARK, M. JAFFE, J. R. and N. R. LANGLEY, *Ceram. Engng. and Sci. Proc.* **7** (1986) 901.
14. T. ISIKAWA, H. ISHIKAWA and H. TERANISHI, High Temp. Mater. Chem. IV, Proceeding of the Electrochem. Soc. (1988) 205.
15. M. H. JASKOWIAK and J. A. DI CARLO, *J. Amer. Ceram. Soc.* **72** (1989) 192.
16. B. A. BENDER, J. S. WALLACE and D. J. SCHRODT, *J. Mater. Sci.* **26** (1991) 970.
17. T. YAMAMURA, T. ISHIRKAWA, M. SHIBUYA, T. HISAYUKI and K. OKAMURA, *J. Mater. Sci.* **23** (1988) 2589.
18. D. B. FISBACH, P. M. LEMOINE and G. V. YEN, *ibid.* **23** (1988) 9987.
19. R. CHAIM, A. H. HEUER and R. T. CHEN, *J. Amer. Ceram. Soc.* **71** (1988) 960.
20. R. BODET, N. JIA and R. E. TRESSLER, *ibid.* **76** (1993) 3051.
21. D. MOCAER, R. PAILLER, R. NASLAIN, C. RICHARD, J. P. PILLOT and J. DUNOGUES, *J. Mater. Sci.* **28** (1993) 2632.
22. D. MOCAER, R. PAILLER, R. NASLAIN, C. RICHARD, J. P. PILLOT, J. DUNOGUES, O. DELVERDIER and M. MONTHIOUX, *ibid.* **28** (1993) 2639.
23. W. TOREKI, C. D. BATICH, M. D. SACKS, M. SALEEM, G. J. CHOI and A. A. MORONNE, *Comp. Sci. Tech.* **51** (1994) 145.
24. Y. HASEGAWA, *ibid.* **51** (1994) 161.
25. D. C. DELEEUW and J. LIPOWITZ, Eur. Pat. N° 0 438 117 A1, Jan. 15 (1991).
26. J. LIPOWITZ, J. A. RABE and G. A. ZANK, *Ceram. Engng. Sci. Proc.* **12** (1991) 1819.
27. J. LIPOWITZ, T. BARNARD, D. BUJALSKI, J. A. RABE, G. A. ZANK, A. ZANGVIL and Y. XU, *Comp. Sci. Tech.* **51** (1994) 167.
28. Y. XU, A. ZANGVIL, J.LIPOWITZ, J. A. RABE and G. A. ZANK, *J. Amer. Ceram. Soc.* **76** (1993) 3034.
29. K. OKAMURA, M. SATO, T. SEGUSHI and S. KAWANISHI, in "Composite Materials" edited by H. Ishida (Elsevier, New York, 1990) p. 209.
30. M. TAKEDA, Y. IMAI, H. ICHIKAWA T. ICHIKAWA, T. SEGUSHI and K. OKAMURA, *Ceram. Engng. Sci. Proc.* **12** (1991) 1007.
31. M. TAKEDA, Y. IMAI, H. ICHIKAWA, T. ICHIKAWA, N. KASAI, T. SEGUSHI and K. OKAMURA, *ibid.* **13** (1992) 209.
32. *Idem*, *ibid.* **14** (1993) 540.
33. T. ICHIKAWA, *Comp. Sci. Tech.* **51** (1994) 135.
34. J. F. VILLENEUVE, D. MOCAER, R. PAILLER, R. NASLAIN and P. OLRY, *J. Mater. Sci.* **28** (1993) 1227.
35. R. BODET, J. LAMON, N. JIA and R. E. TRESSLER, *J. Amer. Ceram. Soc.* (in press).
36. C. GERARDIN, M. HENRY and F. TAULELLE, Mat. Res. Soc. Symp. Proc., Vol. 271, 1992, edited by M. J. Hampden-Smith, W. G. Klemperer and C. J. Brückner, San Francisco. (Better Ceramics through Chemistry, V) 243–8.
37. R. BODET, X. BOURRAT, J. LAMON and R. NASLAIN, *J. Mater. Sci.* **30** (1995) 661.
38. F. LAANANI, M. MONTHIOUX, C. GUIMON, G. CHOLLON and R. PAILLER, *J. Eur. Ceram. Soc.* (in press).
39. P. LESPADE, A. MARCHAND, M. COUZI and F. CRUEGE, *Carbon* **22** (1984) 375.
40. F. TUINSTRA and J. L. KOENIG, *J. Chem. Phys.* **53** (1970) 1126.
41. M. RICCI, thesis n°644, University of Bordeaux I (1991).
42. E. BOUILLON, F. LANGLAIS, R. PAILLER, R. NASLAIN, J. C. SARTHOU, A. DELPUECH, C. LAFFON, P. LAGARDE, F. CRUEGE, P. V. HUONG, M. MONTHIOUX and A. OBERLIN, *J. Mater. Sci.* **26** (1991) 1333.
43. E. BOUILLON, R. PAILLER, R. NASLAIN, E. BAQUE, M. BIROT, J. P. PILLOT, J. DUNOGUES and P. V. HUONG, *Chem. Mater.* **3** (1991) 356.
44. Y. SAZAKI, Y. NASHINA, M. SATO and K. OKAMURA, *J. Mater. Sci.* **22** (1987) 443.
45. R. J. DAY, V. PIDDOCK, R. TAYLOR, R. J. YOUNG and M. ZAKIKHANI, *ibid.* **24** (1989) 2898.
46. P. MARTINEAU, M. LAHAYE, R. PAILLER, R. NASLAIN, M. COUZI and F. CRUEGE, *ibid.* **19** (1984) 2731.
47. K. GOHLERT, G. IRME, L. MICHLOWSKY and J. MONECKE, *Mat.-wiss. u. Werckstofftech.* **21** (1990) 108.
48. P. DELHAES, internal report, Rhone Poulenc, Centre de Recherche Paul Pascal, Pessac Fr. (1987).
49. O. CHAUVET, L. ZUPPIROLI and I. SOLOMON, *Mater. Sci. and Engng.* **B11** (1992) 303.
50. P. ROCABOIS, thesis, Institut National Polytechnique de Grenoble (1993).
51. W. D. KINGERY, H. K. BOWEN and D. R. UHLMANN, in "Introduction to Ceramics", edited by E. Burke, B. Chalmers and J. A. Krumshansl (John Wiley & Sons, New York, 1975) p. 448.
52. E. A. GULBRANSEN and S. A. JANSSON, *Oxidation of Metals* **4** [3](1972) 181.
53. W. V. Van RIJSWICK, *J. Amer. Ceram. Soc.* **73** (1990) 148.
54. S. PROCHAZKA and R. J. CHARLES, *Amer. Ceram. Soc. Bull.* **52** (1973) 885.
55. A. CHRYSANTHOU, P. GRIEVESON and A. JHA, *J. Mater. Sci.* **26** (1991) 3463.
56. T. SHIMOO, T. HAYATSU, M. NARISAWA, M. TAKEDA, H. ICHIKAWA, T. SEGUSHI and K. OKAMURA, *J. Ceram. Soc. Jpn.* **101** (1993) 1379.
57. J. S. HARTMAN, M. F. RICHARDSON, B. L. SHERIFF and B. G. WINSBORROW, *J. Amer. Chem. Soc.* **109** (1987) 6059.
58. G. D. SORARU, F. BABONNEAU and J. D. MACKENSIE, *J. Mater. Sci.* **25** (1990) 3886.
59. C. GERARDIN, thesis, University of Paris IV (1991).
60. P. DELHAES and F. CARMONA, *Chem. Phys. Carbon* **17** (1981) 89–174.
61. A. OBERLIN, *ibid* **22** (1989) 1.
62. B. E. DEAL and A. S. GROVE, *J. Appl. Phys.* **36** (1965) 3770.
63. P. J. JORGENSEN, M. E. WADSWORTH and I. B. CUTLER, *J. Amer. Ceram. Soc.* **42** (1959) 613.
64. J. A. COSTELLO and R. E. TRESSLER, *ibid.* **64** (1981) 327.

65. *Idem*, *ibid*. **69** (1986) 674.
66. Z. ZHENG, R. E. TRESSLER and K. E. SPEAR, *Corrosion Sci*. **33** (1992) 569.
67. S. A. NEWCOMB, K. E. SPEAR and R. E. TRESSLER, Annual Review of the Center for Advanced Materials, Vol. III: GRI-Properties, Processing and Fabrication Technologies, Pennsylvania State University, Sept. 13 (1994).
68. S. C. SINGHAL, *J. Mater. Sci.* **11** (1976) 1246.
69. R. WARREN and C.H. ANDERSON, *Composites* **15** (1984) 101.
70. T. J. CLARK, E. R. PRACK, M. I. AIDER and L. C. SAWYER, *Ceram. Engng. Sci. Proc.* **7** (1986) 901.
71. L. FILIPUZZI and R. NASLAIN, Proceedings of the 7th CIMTEC, Mater. Sci. Monograph 68 Adv. Structural Inorg. Composites, edited by P. Vincenzini (Elsevier, Amsterdam, 1991) p. 35.
72. T. SHIMOO, H. CHEN and K. OKAMURA, *J. Ceram. Soc. Jpn.* **100** (1992) 929.
73. D. MOCAER, G. CHOLLON, R. PAILLER, L. FILIPUZZI and R. NASLAIN, *J. Mater. Sci.* **28** (1993) 3059.
74. T. SHIMOO, T. HAYATSU, M. TAKEDA, H. ICHIKAWA, T. SEGUSHI and K. OKAMURA, *J. Ceram. Soc. Jpn.* **102** (1994) 617.
75. F. J. NORTON, *Nature* **171** (1961) 701.

Received 19 April
and accepted 21 May 1996